Characteristics and Dynamics of wind-driven upwelling in the Alaskan Beaufort Sea based on six years of mooring data

Peigen Lin[1,2], Robert S. Pickart[2], G.W.K. Moore[3], Michael A. Spall[2], Jianyu Hu[1]

October 2017

Revised for Deep-Sea Research II

Corresponding Author: Peigen Lin (plinwhoi@gmail.com)

---

[1] *State Key Laboratory of Marine Environmental Science, College of Ocean and Earth Sciences, Xiamen University, Xiamen, Fujian 361102, China*

[2] *Woods Hole Oceanographic Institution, Woods Hole, MA 02540, USA*

[3] *Department of Physics, University of Toronto, Toronto, Ontario, Canada.*

Abstract

Six years of mooring data from the Alaskan Beaufort Sea slope, together with meteorological observations and reanalysis fields, are used to quantify the occurrence of wind-driven upwelling and the associated atmospheric forcing. The canonical upwelling event, composited from 115 individual events, reveals that when the easterly wind is strongest the entire shelfbreak jet is reversed to the west. At the end of the event a bottom-intensified, eastward-flowing "rebound jet" spins up that is stronger than the normal shelfbreak jet. The cross-isobath flow has a three-layer structure with onshore flow in the surface layer, offshore flow in the middle of the water column, and onshore flow near the bottom. This is because the reversed shelfbreak jet is oriented slightly onshore which overwhelms the cross-isobath surface Ekman transport. The vertically-integrated along-isobath momentum balance supports this interpretation and also indicates that the rebound jet is driven by the zonal gradient in sea surface height. During over two thirds of the events Atlantic water (AW) is upwelled to the shelfbreak, while for the remaining events only Pacific water (PW) is upwelled. The primary driving factor behind this is the seasonal variation in the PW-AW interface depth offshore of the shelfbreak, which is controlled by the local wind stress curl. During summer, when PW-type events dominate, Ekman pumping associated with negative wind stress curl deepens the interface depth, limiting access to the Atlantic layer. Over the remainder of the year, when AW events dominate, Ekman suction associated with positive wind stress curl raises the interface. These variations are due to the influence of the two regional atmospheric centers of action — the Aleutian Low and the Beaufort High.

Keywords: upwelling, Beaufort Shelfbreak jet, shelf-basin exchange, atmospheric centers of action

1. Introduction

It has long been known that upwelling occurs in the Alaskan Beaufort Sea, driven by easterly winds (Hufford, 1974). The upwelling takes place throughout the year during a variety of ice conditions. Using two years of mooring data together with meteorological records, Schulze and Pickart (2012) demonstrated that roughly 95% of strong storms (where easterly wind speeds exceed 10 m s^{-1}) result in upwelling. Based on this empirical relationship, Pickart et al. (2013a) used the 70-year wind record from the Barrow, AK weather station to characterize long-term trends in such strong upwelling storms. According to this proxy, in recent decades upwelling events have increased in both number and strength. In addition, Pickart et al. (2013a) determined that there are two seasonal peaks of upwelling occurrence associated with enhanced easterly winds, one in spring (May) and a second in fall (November). However, these two peaks have shifted in recent years: the spring peak is now later (June), and the fall peak earlier (October), associated with a corresponding shift in alongcoast windspeed (Lin et al., 2016).

Wind conditions in the Alaskan Beaufort Sea are primarily dictated by the behavior of two atmospheric centers of action – the Aleutian Low and the Beaufort High (Pickart et al., 2013a; Brugler et al., 2014). The latter is a semi-stationary region of high pressure situated in the central Beaufort Sea (Reed and Kunkel, 1960; Walsh, 1978), which gives rise to easterly winds in the southern Beaufort Sea. Lin et al. (2016) demonstrated that the Beaufort High is the main driver of upwelling during the warm months of the year, consistent with the results of Watanabe (2013) and Pickart et al. (2013a). The Aleutian Low is the integrated signature of low pressure systems transiting along the north Pacific storm track (Wilson and Overland, 1986; Zhang et al., 2004). During the passage of such storms, easterly winds in the southern Beaufort Sea are often enhanced. The Aleutian Low becomes deeper in the fall and winter (Favorite et al., 1976). While this

contributes to the autumn wind peak noted above, both centers of action play a role during the cold months of the year (Pickart et al., 2013b; Lin et al., 2016).

While upwelling can occur in any month of the year, it is strongly modulated by the presence of sea ice (Schulze and Pickart, 2012). Since mobile pack ice is able to transmit wind stress to the water column (Røed and O'Brien, 1983), upwelling readily occurs when the sea surface is only partially covered by ice. In fact, Schulze and Pickart (2012) found that upwelling was strongest during the shoulder ice seasons (late-spring and late-fall). This is in line with the numerical results of Martin et al. (2014) and the observations of Pickart et al. (2013b). The reason for this is that the momentum flux from the atmosphere to the ocean is stronger via freely-moving ice keels (Häkkinen, 1986; Pite et al., 1995). Notably, upwelling at the Beaufort shelfbreak occurs even when the ice concentration is 100%, as long as the pack ice is mobile (Schulze and Pickart, 2012).

Wind-driven upwelling is one of the primary mechanisms of shelf-basin exchange in the Alaskan Beaufort Sea. The resulting cross-stream circulation transfers heat and freshwater offshore into Canada Basin (Yang, 2006). According to Pickart et al. (2013b), a single (strong) storm can flux enough heat offshore to melt an area of 1-m thick ice the size of the Beaufort shelf. At the same time, the freshwater fluxed offshore is enough to significantly influence the year-to-year variations in the freshwater content of the Beaufort Gyre (Proshutinsky et al., 2002, 2009). In addition to these physical effects, the wind-driven exchange has ramifications for the regional ecosystem as well. Nutrients are upwelled from the basin (Pickart et al., 2013b) that could impact primary production on the Beaufort shelf (Macdonald et al., 2010). This in turn provides food for Arctic cetaceans (e.g. Okkonen et al., 2011).

The boundary current system of the Beaufort Sea consists of two components. The first is the Beaufort shelfbreak jet, which is variously referred to in the literature as the western Arctic

93 boundary current (Nikolopoulos et al., 2009), or the Pacific-water boundary current. As reported
94 in previous studies (e.g. von Appen and Pickart, 2012; Brugler et al., 2014), the shelfbreak jet
95 advects both Pacific summer water and winter water, the latter of which contains high
96 concentrations of nutrients (Lowry et al., 2015). In late-summer the current is surface-intensified
97 and transports very warm and fresh Alaskan coastal water. The rest of the year it is bottom-
98 intensified and advects Bering Sea summer water (in early-summer and again in early-autumn)
99 and winter water (the remainder of the year). The eastward volume flux, heat flux, and freshwater
100 flux are all greatest in summer when the current is surface-intensified (Brugler et al., 2014). This
101 is consistent with studies on the Chukchi shelf indicating that, in summer, much of the Pacific
102 water emanating from the Bering Strait exits the shelf through Barrow Canyon (Itoh et al., 2012;
103 Gong and Pickart, 2016; Pickart et al., 2016, Weingartner et al., 2017).

104 The second component of the Beaufort Sea boundary current system is the eastward-flowing
105 Atlantic water located downslope and offshore of the shelfbreak jet. On average, the Atlantic water
106 resides deeper than 180 m beneath the layer of Pacific winter water (Nikolopoulos et al., 2009).
107 The Atlantic water is a part of the large-scale cyclonic boundary current system of the Arctic Ocean
108 (Aagaard, 1984; Rudels et al., 2004; Karcher et al., 2007; Aksenov et al., 2011). Presently its
109 eastward transport in the Canada Basin is unknown. This is because, unlike the shelfbreak jet, it
110 has not been adequately sampled by moorings. Only the inshore portion of the current has been
111 documented observationally (Nikolopoulos et al., 2009).

112 During easterly wind events the shelfbreak jet typically reverses to the west, followed a short
113 time later by upwelling of water from the basin to the shelf (Pickart et al., 2009, 2013b). In some
114 cases the upwelled water is Pacific water, while at other times warm and salty Atlantic water is
115 also upwelled (Schulze and Pickart, 2012). To date, the reasons dictating one scenario versus the

other have not been explored. Using data from a cross-stream array of 7 moorings spanning the outer Beaufort shelf to the mid-continental slope, Pickart et al. (2011, 2013b) diagnosed a single event that occurred in November 2012. This revealed that, while the isopycnals in the upper part of the water column were deflected upward onto the shelf during the event, the deeper isopycnals were deflected downwards. This highlights the fact that the upwelling is not simply a two-dimensional process. Furthermore, during the relaxation phase of the November 2012 event, a deep eastward-flowing jet was spun up, temporarily enhancing the flow of Atlantic water. It remains to be determined if both of these features are ubiquitous to upwelling on the Beaufort slope.

In this paper we use 6 years of mooring data to quantify various aspects of upwelling across the Beaufort shelfbreak. The first two years of data (2002 – 2004) come from the mooring array noted above, while the remaining four years (2008 – 2012) are from a single mooring deployed in the center of the Beaufort shelfbreak jet. With this amount of data, we can, for the first time, construct and diagnose a composite upwelling event and quantify the hydrographic response as well as the primary and secondary circulation. Two of the major aims of our study are to understand the cross-isobath flow during an upwelling event, and determine the underlying reason why some of the events advect only Pacific water onto the shelf, while others flux Atlantic water as well. In doing so we elucidate the role of the atmospheric forcing, both on synoptic timescales as well as seasonally.

The location of the mooring array (and the single mooring in the later years) corresponds to one of the designated sections of the Distributed Biological Observatory (DBO) program. As described by Moore and Grebmeier (this issue), DBO is designed to detect and ultimately understand ongoing changes to the ecosystem of the Pacific Arctic. Towards this end, eight

139 locations have been identified, spanning the region from the northern Bering Sea to the Canadian
140 Beaufort Sea, where targeted measurements are being carried out by the international community.
141 This includes shipboard sampling via dedicated programs or cruises of opportunity, as well as
142 mooring measurements. The specific locations were chosen in part due to enhanced biological
143 activity in the water column and/or the sediments. The mooring data described in the present study
144 were collected at the DBO-6 line, which crosses the Alaskan Beaufort shelf/slope approximately
145 150 km east of Barrow Canyon (see Moore and Grebmeier (this issue) for the locations of the eight
146 DBO lines). This region is characterized by significant shelf/basin exchange due to both external
147 forcing (wind) and internal forcing (instabilities of the flow). As such, the present study serves to
148 inform the DBO community regarding various aspects of the wind-driven exchange at this location
149 and its potential impacts on the ecosystem.
150
151 **2. Data and methods**
152 *2.1. Mooring array data in 2002–2004*
153 A mooring array was maintained across the Alaskan Beaufort shelfbreak and slope (near
154 152°W) from August 2002 to early September 2004 as part of the Western Arctic Shelf-Basin
155 Interactions (SBI) program (Fig.1). There were 8 moorings named BS1–BS8 from onshore to
156 offshore (BS6 was only available from August 2002 to early September 2003). In this study we
157 only use moorings BS2–BS7. The velocity was recorded hourly using upward-facing acoustic
158 Doppler current profilers (ADCP, RDI 75 KHz) with a vertical resolution of 5–10 m at moorings
159 BS2–BS6. Hydrographic traces were obtained 2–4 times per day using a coastal moored profiler
160 at these sites and a McLane moored profiler at BS7. These profilers are motorized conductivity-
161 temperature-depth (CTD) instruments that provide vertical profiles with 2 m resolution spanning

from the top float of the mooring (at roughly 40 m depth) to near the bottom. Velocity at mooring BS7 was measured using an acoustic travel-time current meter that was part of the profiler. Hourly point CTD measurements were collected at all of the sites using MicroCats, which were situated just below the deepest profiler depth. The reader should consult Fratantoni et al. (2006), Spall et al. (2008), and Nikolopoulos et al. (2009) for details of the instrumentation on the moorings, including the calibration procedures and measurement accuracies.

2.2. Single mooring data in 2008–2012

One of the moorings in the array, BS3 (blue star in Fig. 1), which is in the center of the Beaufort shelfbreak jet, has been subsequently deployed since August 2008 as part of the Arctic Observing Network (AON). The deployments were similar to that in the years 2002–2004. As seen in Table 1, the top float was situated between 35–40 m, and the upward-facing RDI 75 KHz ADCP and MicroCat were located at 128 m depth (roughly 20 m above the bottom). The vertical range of the coastal moored profiler had small changes from year to year depending on the top float depth. Starting in 2009 a second upward-facing ADCP (RDI 300 kHz) was attached to the top float along with an additional MicroCat. The vertical resolution of the shallow velocity profile was 5–10 m. We interpolated the velocity data using both ADCPs in 2009–2011 when the top instrument returned good data, otherwise only data from the 75 kHz instrument were used (whose range extended close to the surface).

2.3. Meteorological data

Wind data used in this study are from the meteorological station in Barrow, AK (Fig. 1), which is the closest weather station to the mooring array. Previous studies (e.g. Nikolopoulos et al., 2009; Pickart et al., 2009) have demonstrated that the winds at Barrow are a good proxy for those at the array site. The data were obtained from the National Climate Data Center of the

National Oceanic and Atmospheric Administration (http://www.ncdc.noaa.gov/), and have been quality controlled and interpolated to a one-hour temporal resolution (see Pickart et al., 2013a).

2.4. Atmospheric reanalysis data

We use wind stress and sea-level pressure (SLP) data from the Arctic System Reanalysis (ASR) version 1, which has a 30 km grid spacing and 3-hourly temporal resolution, available at NCAR Research Data Archive (https://climatedataguide.ucar.edu/climate-data/arctic-system-reanalysis-asr). The ASR is based on the Polar WRF model with boundary conditions provided by the Interim Reanalysis from the ECMWF (ERA-I) (Bromiwich et al., 2015). A comparison of surface and 500 mb observations between the ERA-I and ASR version 1 during 2007 found similar annual mean biases, with the ASR generally having smaller root-mean-square errors and higher correlations (Bromwich et al., 2015). Comparing the ASR with the ERA-I in the Greenland region, Moore et al. (2016) found that the ASR was more accurate for both high and low wind speeds, with a smaller root-mean-square error between the reanalysis winds and observations. We also use the ASR fields to compute timeseries of wind stress curl.

208 Table 1. Configuration of mooring BS3 in 2008–2012

		2008–2009	2009–2010	2010–2011	2011–2012
Top float	Depth (m)	40	40	35	35
ADCP at top float	Vertical resolution (m)	No instrument	10	5	Failed
ADCP near bottom (128 m)	Vertical resolution (m)	5	5	10	10
Moored Profiler	Vertical measuring range (m)	44–127	44–127	40–126	40–126

209

210

211 **3. Wind-driven upwelling events**

212 We begin our study by objectively defining what we mean by a wind-driven upwelling event
213 and comparing this to different wind metrics. We then construct a composite event using our 6
214 years of data, which enables us to robustly explore various aspects of upwelling on the Beaufort
215 slope. Wind-driven upwelling is assumed to take place at the mooring site when the near-bottom
216 potential density at mooring BS3 is greater than the climatological monthly mean value (where the
217 climatology is computed over the 6-year record), and the mean alongcoast (105°T) wind is easterly
218 (negative) over the upwelling period. On average, the hydrographic response of the water column
219 lags the alongcoast wind by t_d = 21 h, which was taken into account when computing the event-
220 mean alongcoast windspeed. A small fraction of upwelling events, with duration less than a day,
221 had only a minor effect on the water column and hence are not considered in the study. Furthermore,

222 we exclude events that lasted more than 17 days (12% of the events), because it was ambiguous if
223 some of these were actually due to back-to-back storms (excluding these long events did not
224 appreciably impact our results). Accordingly, a total of 115 upwelling events were identified over
225 the 6-year record. The events occurred in all seasons, which is in line with previous studies (e.g.
226 Schulze and Pickart, 2012).

227 *3.1. Effect of wind*

228 To clarify the effect of the alongcoast wind on the upwelling events, we quantified the
229 strength of each event by defining an upwelling index (UI) which is the time integral of the near-
230 bottom potential density anomaly (i.e. subtracting out the climatological monthly mean) over each
231 event. This definition accounts for both the magnitude and duration of the events. As an indicator
232 of the alongcoast wind, the cumulative Ekman transport (Huyer et al., 1979) for each event was
233 computed,

234 $$T_{CE} = \int_{t_s - t_d}^{t_e - t_d} \tau_s(t) dt \,/(\rho_0 f), \quad (1)$$

235 where t_s and t_e are the start and end time of each upwelling event, respectively, τ_s is the wind stress,
236 f is the Coriolis parameter, and ρ_0= 1025 kg m^{-3} is the reference density. Similar to the upwelling
237 index, T_{CE} takes into account the magnitude and length of the storm, and has been used in other
238 studies as a measure of the wind-driven secondary circulation (e.g. Pisareva et al., 2015).
239 Comparing UI and T_{CE} for all of the upwelling events over the six-year period, we find that the
240 two quantities are significantly correlated (R=0.71, with a confidence level of > 95%, Fig. 2a).
241 This indicates that more offshore cumulative Ekman transport is generally associated with stronger
242 upwelling, which is not surprising. The best fit regression (black line), $\log(\mathrm{UI}) = 0.62 \times$
243 $\log(T_{CE}) - 1.66$, suggests a linear model for predicting UI from alongcoast wind.

In addition to the Ekman transport driven by the easterly wind, we consider the Ekman pumping. In particular, we computed the mean local wind stress curl for each upwelling event using the ASR data (the data points near mooring BS3), and compared this to the corresponding value of UI (Fig. 2b). There is no obvious relationship between the upwelling index and the wind stress curl. In general, positive wind stress curl is upwelling-favorable and negative curl is downwelling-favorable. However, over the 6-year record, more than 50% (64 of 115) of the upwelling events occurred with negative wind stress curl. Furthermore, for the strongest upwelling events (UI > 180), the wind stress curl was close to zero. We also integrated the wind stress curl around the mooring BS3 during each upwelling event (not shown), which does not change the result. This implies that the upwelling in our study region is not related to the local wind stress curl, but instead is associated with coastal upwelling, which is consistent with the modeling results of Pickart et al. (2011).

3.2. General characteristics of upwelling

To investigate the general features of upwelling, we constructed a composite event by averaging together the 115 individual events. The mean (median) duration of the events was 4.8 (2.9) days, and 68% of the events were shorter than 5 days. We defined a normalized time, t_n, which ranges from 0 at the beginning of the event to 1 at the end (recall that an event is defined as the time period over which the near-bottom potential density anomaly exceeds zero during easterly winds). We consider as well the conditions just prior to and after the upwelling ($-0.25 \leq t_n \leq 1.25$). Figure 3 displays the composites of alongcoast windspeed and near-bottom potential density anomaly. Since each of the events are independent, the uncertainties are reported as standard errors (in this figure and subsequent figures). One sees that, on average, the wind intensifies prior to the onset of upwelling and peaks at 5.3 m s^{-1} shortly after the upwelling begins (roughly at t_n=0.1).

267 This is consistent with the results of Schulze and Pickart (2012) who found (using only two years
268 of data) that upwelling often commenced when the easterly wind speed exceeded 4 m s^{-1}. After
269 peaking, the wind falls steadily during the remainder of the event to speeds less than 1 m s^{-1} at the
270 end. The potential density anomaly for the composite event reaches values near 0.5 kg m^{-3}, peaking
271 near t_n=0.4. This is consistent with the above result that there is a delay between the wind forcing
272 and the upwelling response. Note that, after the event, the density anomaly falls to the same level
273 as prior to the upwelling.

274 We also computed various hydrographic fields for the composite upwelling event (Fig. 4).
275 Prior to the event, cold Pacific water is present in the lower part of the water column. This layer is
276 lifted at the mooring site during the event and also warms, indicative of enhanced mixing.
277 Interestingly there is an asymmetry in that a larger amount of winter water resides on the upper
278 slope after the event ends. During the upwelling, the deep isohalines (and isopycnals) are quickly
279 raised approximately 20 m by t_n = 0.1. Notably, for the composite event, only a small amount of
280 Atlantic water appears at the base of the mooring from t_n = 0.25 – 0.6 (this is based on the Pacific-
281 Atlantic water boundary from Nikolopoulos et al. (2009)). The distribution of buoyancy frequency
282 reveals that the upwelled dense Pacific water has enhanced stratification, and the middle portion
283 of the water column, from 40 to 60 m, also becomes more strongly stratified (note that our
284 hydrographic measurements only extend to 40 m).

285 *3.3. Velocity structure of upwelling*

286 Using the ADCP data at mooring BS3 we computed composites of the along-isobath and
287 cross-isobath velocities (Fig. 5). The along-isobath direction was chosen to be 125°T, based on the
288 IBCAO v3 bathymetric product. Positive (negative) values refer to eastward (westward) in the
289 along-isobath direction and offshore (onshore) in the cross-isobath direction, respectively. This is

290 also the direction of the year-long mean eastward-flowing shelfbreak jet (Nikolopoulos et al.,
291 2009). One sees that the depth-averaged current reverses during the first part of the upwelling
292 event when the easterly winds are strongest (compare Fig. 5a to Fig. 3a). The peak speed reaches
293 0.1 m s^{-1}. For an average current width of 15 km (Brugler et al., 2014) and depth of 150 m, this
294 results in a temporary westward transport of 0.22 Sv, which is roughly two times larger than the
295 undisturbed eastward transport of the jet (Nikolopoulos et al., 2009).

296 The depth-dependent along-isobath velocity (Fig. 5b) reveals that, prior to the onset of
297 upwelling, the eastward-flowing shelfbreak jet is bottom-intensified (~ 0.1 m s^{-1}), while the flow
298 in the upper layer has already been reversed. This is due to the intensifying easterly winds. Such a
299 short response time of the shelfbreak jet to the winds is consistent with the statistical analysis of
300 Pickart et al. (2009) who computed a time lag of 8 hours, which is on the order of the inertial
301 timescale. By the time the upwelling commences, the shelfbreak jet has been completely reversed
302 and the westward flow reaches its peak speed (exceeding 0.15 m s^{-1} in the surface layer) around t_n
303 = 0.1. This is near the peak of the wind, indicating that the velocity responds very quickly to the
304 easterly winds. About half way through the event the shelfbreak jet starts to re-establish at depth,
305 and, at the end of the event, it is much stronger (0.20 m s^{-1}) than it was before the storm. This is in
306 line with the results of Pickart et al. (2011) who analyzed a single upwelling event in November
307 2002. They demonstrated that an eastward-flowing "rebound" jet spun up at the end of the event
308 which transported Atlantic water eastward. This was due to the discrepancy in timescales of the
309 sea surface height response to changes in the wind versus the baroclinic water column response.
310 Our composite event demonstrates that the development of the post-storm rebound jet is a
311 ubiquitous feature of the Beaufort slope.

312 The depth-averaged cross-isobath velocity (Fig. 5c) is onshore over most of the event, with
313 a peak speed of 0.02 m s^{-1}. The depth-dependent structure (Fig. 5d) is that of onshore flow in the
314 upper 60 m, offshore flow beneath this (to ~110 m), and onshore flow in the bottom layer. (Recall
315 that the ADCP is situated roughly 20 m above the bottom, so our measurements do not capture the
316 near-bottom flow.) The onshore flow at depth is of course required for the upwelling. This three-
317 layer structure is different than the Ekman-like secondary circulation pattern described by Schulze
318 and Pickart (2012) and Pickart et al. (2013b) during upwelling at this location. There are two
319 important differences, however, between those analyses and ours. The earlier studies defined an
320 alongstream coordinate system aligned with the mean transport vector (i.e. the flow averaged both
321 vertically and laterally across the current), which changes orientation from storm to storm (Schulze
322 and Pickart, 2012) and even within a single storm (Pickart et al., 2013b). Here we are interested in
323 the upwelling that (by definition) takes place across the isobaths, hence we align our coordinate
324 system with the bathymetry. The previous studies also considered the region of the outer shelf
325 which is shoreward of the core of the shelfbreak jet. In such a coordinate frame the secondary flow
326 on the outer shelf is accurately predicted by Ekman theory (Pickart et al., 2013b). However, it is
327 evident by comparing Figs. 5b and 5d that, for the composite event presented here, the reversed
328 shelfbreak jet is oriented slightly onshore. That is, some of the westward alongstream flow is
329 folded into the cross-isobath component. This likely overcomes the Ekman flow directed seaward
330 across the isobaths in the surface layer.
331 To elucidate this further, we diagnosed the vertically integrated along-isobath momentum
332 balance. Due to the fact that we have only a single mooring, we are unable to evaluate the
333 divergence of the along-isobath momentum flux (along-isobath DMF) or cross-isobath momentum
334 flux (cross-isobath DMF). To assess the magnitude of the former, we estimated the convergence

of the isobaths along the upper slope in the vicinity of the mooring using the IBCAO v3 bathymetric data set. Assuming that the transport is conserved along the slope, this results in a small along-isobath change in the current speed, implying that this term is on average only ~15% of the wind stress term and thus can be ignored. With regard to the cross-isobath DMF, using data from the full SBI mooring array Pickart et al. (2013b) calculated this quantity for a single upwelling event. They found that this force acted in the same manner as the surface stress term in reversing the shelfbreak jet, but was roughly 3/4 of the magnitude. As such, we assume that it has the same functional form as the wind stress calculated below but is smaller by 25%. (We note that Pickart et al. (2013b) evaluated the force balance a bit shoreward of the core of the shelfbreak jet.)

The terms in the momentum balance can be written as

$$\overbrace{\frac{\partial}{\partial t}\int_{-h}^{0} u\,dz}^{Acceleration} + \overbrace{\frac{\partial}{\partial y}\int_{-h}^{0} uv\,dz}^{DMF} - \overbrace{f\int_{-h}^{0} v\,dz}^{Coriolis} + \overbrace{\frac{1}{\rho_0}\int_{-h}^{0}\frac{\partial p}{\partial x}dz}^{PGF} - \overbrace{\frac{\tau_{sx}}{\rho_0}}^{Wind\ stress} + \overbrace{\frac{\tau_{bx}}{\rho_0}}^{bottom\ stress} = 0, \quad (2)$$

where x and y are the along-isobath and cross-isobath directions, respectively; u and v are the corresponding depth-dependent velocities; f is the Coriolis parameter; and ρ_0= 1025 kg m^{-3} is the reference density. The terms on the left-hand side of (2) are the local acceleration of the vertically-integrated along-isobath velocity, the cross-isobath DMF, the Coriolis force, the along-isobath pressure gradient force (PGF), the wind stress (τ_{sx}), and the bottom stress (τ_{bx}). The along-isobath PGF is determined as the residual (see also Pickart et al., 2013b). We assume a linear drag law to estimate the bottom stress (Pringle, 2002):

$$\tau_{bx} = \rho_0 r U/H, \quad (3)$$

where H is the water depth, and $r \approx 5 \times 10^{-4}$ m s^{-1}.

The evolution of the terms in (2) during the normalized upwelling event are presented in Fig. 6. Note that all of them are close to zero before and after the event (at t_n=-0.25 and t_n=1.25). The

357 acceleration term reflects the spinning up of the reversed jet followed by the re-establishment of
358 the eastward-flowing shelfbreak jet, and, finally, the acceleration of the rebound jet. Before the
359 upwelling begins, the wind stress and bottom stress are the same sign, but once the jet reverses
360 through the water column they tend to balance each other. As such, the Coriolis force is largely
361 responsible for the continued reversal of the along-isobath flow.

362 Through roughly the first three quarters of the upwelling period the PGF tends to offset the
363 Coriolis force. This is a reflection of the fact that the reversed jet is in geostrophic balance; in
364 particular, the sea surface height is higher offshore of the jet (e.g. Pickart et al., 2013b). As noted
365 above, the orientation of the reversed jet is such that a component of the alongstream flow is
366 directed across the isobaths over this time period. Hence a signature of the cross-stream
367 geostrophic balance is manifested in the along-isobath force balance. During the last part of the
368 event the Coriolis force in Fig. 6 goes to zero and the PGF largely balances the local acceleration
369 – which becomes larger at this time. This corresponds to the spin up of the rebound jet (Fig. 5b),
370 and our interpretation is that the PGF is now mostly due to a west-to-east drop in sea surface height
371 (consistent with the conclusions of Pickart et al., 2013b). Overall then, we argue that the cross-
372 isobath flow during the composite upwelling event is not Ekman-like because of the orientation of
373 the reversed jet, and that the large-scale zonal gradient in sea level drives the rebound jet at the
374 end of the event. Both of these notions are consistent with the vertically integrated momentum
375 balance.

376

377 **4. Upwelling of Atlantic water versus Pacific water**

378 As discussed in the introduction, during some upwelling events Atlantic water (AW) is
379 advected onto the shelf, while the remaining events are characterized by only Pacific water (PW)

in the near-bottom layer. This was noted by Schulze and Pickart (2012) using the BS2 mooring data on the outer shelf from 2002 – 2004. However, they did not consider the reasons behind the different cases. In this study we have 6 years of data available at mooring BS3, just seaward of the shelfbreak. We now investigate what dictates the two types of upwelling, which we refer to as AW-type and PW-type, respectively. Over the 6-year time period, 85 of the 115 upwelling events were AW-type, and the remaining 30 events were PW-type. This means that upwelling of AW occurs about three times more frequently than just PW alone.

4.1. Atmospheric forcing

First we investigate the role that the atmospheric forcing has on the type of upwelling. Since the AW resides below the PW in the Canada Basin, one might expect simply that the stronger the winds, the greater the chance of drawing AW to the shelfbreak. This is not true, however.

Previous studies have demonstrated that the winds in the western Beaufort Sea are largely dictated by two atmospheric centers of action, namely the Beaufort High and the Aleutian Low (Pickart et al., 2013a; Brugler et al., 2014; Lin et al., 2016). Using the ASR reanalysis fields, we created composites of the sea level pressure (SLP) and 10-m winds for the AW-type upwelling events and the PW-type events (Fig. 7). For the former (Fig. 7a), a pronounced Beaufort High dominates the Canada Basin, while a deep Aleutian Low is centered over the Alaskan Peninsula (extending over a large portion of the Gulf of Alaska and Bering Sea). The SLP gradient between the two centers of action leads to the easterly winds in our study area. By contrast, PW-type upwelling occurs when the Beaufort High is more confined to the Beaufort Sea with no signature of the Aleutian Low (Fig. 7b). Notably, the strength of the easterly wind at the mooring site is comparable in each case. The timeseries of alongcoast wind for the composite AW- and PW-type upwelling events are similar as well (not shown).

403 Recall the relationship between the upwelling index (UI) and the cumulative Ekman
404 transport (T_{CE}) presented in Section 3.1. In Fig. 2a we have distinguished between the AW- and
405 PW-type events. Consistent with the above result that wind strength does not play a role, both
406 types of events are present over the full range of T_{CE}. However, as is clear from the statistically
407 significant linear fits, PW-type upwelling requires stronger and/or longer wind forcing to attain
408 the same upwelling strength (i.e. near-bottom potential density anomaly) compared to AW-type
409 upwelling. Also, the largest values of UI are all AW events, which is not surprising since AW is
410 denser than PW. These results raise the following question: how does the same strength wind lead
411 to upwelling of Atlantic water in some instances and Pacific water in others? This is addressed
412 below in Section 5.

413 *4.2. Physical attributes*

414 To shed light on the character of the AW- versus PW-type upwelling, we constructed the
415 composite event for each type using the same methodology applied above. Since the majority of
416 the events are AW-type, this composite is qualitatively similar to the full composite (compare Fig.
417 8 to Figs. 4 and 5). One sees in Fig. 8 that Atlantic water is present over much of the event, and
418 the PW-AW interface rises to about 120 m depth. The jet is reversed throughout the water column
419 and is stronger than in the full composite (peaking at 0.2 m s^{-1}). The rebound jet is also stronger.
420 Not surprisingly, the cross-isobath flow in the surface layer is greater as well (in line with the
421 above discussion).

422 The analogous composite fields for the PW-type upwelling show some significant
423 differences (Fig. 9). Much less saline water reaches the shelfbreak (< 33 versus > 34). Another
424 notable difference is that during PW events the hydrographic response is confined to deeper levels:
425 shallower than 80 m the isopycnals remain flat during the event (Fig. 9a). The stratification is also

426 much weaker than during the AW events. Despite the fact that, on average, the wind forcing is
427 similar during both types of events, the shelfbreak jet only reverses in the top 60 m during PW
428 events with a peak westward speed of just 0.07 m s^{-1} compared to 0.2 m s^{-1} for the AW events. The
429 eastward-flowing rebound jet is also weaker. Lastly, the onshore flow in the upper layer is reduced
430 during PW events, and, correspondingly, the offshore flow in the middle of the water column is
431 stronger. The detailed statistics of the two types of events are compared in Table 2.
432
433 Table 2. Statistics of the AW-type and PW-type upwelling events.

	AW-type upwelling (85) (minimum/maximum /mean/standard deviation)	PW-type upwelling (30) (minimum/maximum /mean/standard deviation)
Duration (day)	1.1/14.8/5.2/4	1.0/13.4/3.2/2.8
Density anomaly (kg m^{-3})	0.05/0.85/0.43/0.19	0.03/0.32/0.17/0.08
Isopycnal displacement at BS3 (m)	12.39/47.26/30.56/7.41	8/38.79/28.02/6.13
Buoyancy frequency (10^{-5} s^{-2})	7.28/35.80/14.09/6.09	7.23/20.73/10.02/2.67
Wind speed (m s^{-1})	0.22/8.73/4.09/2.09	0.66/10.70/4.82/2.54
Velocity of reversed flow (m s^{-1})	0.03/0.40/0.15/0.08	0.02/0.20/0.09/0.04

434
435 **5. Seasonal influences on upwelling type**
436 The atmospheric patterns associated with the AW- and PW-type upwelling scenarios (Fig.
437 7) are similar to the seasonal atmospheric composites of Brugler et al. (2014). Those authors
438 divided the year into a cold season (September to February) and warm season (March to August).
439 The former is reminiscent of the AW case, and the latter similar to the PW case (see Fig. 12 of

Brugler et al. (2014)). This implies that seasonality – but not seasonal wind strength – is a main factor driving the type of upwelling that occurs on the Beaufort slope.

Using the 6-year record, we summed up the number of AW- versus PW-type upwelling events for each month (Fig. 10), which reveals a seasonal pattern. Nearly all of the PW events occur in the warm months, particularly in summer (June – August). By contrast, there are relatively few AW events during that time period. Instead, the occurrence of AW events has two peaks: one in spring (March – May) and the other in fall (October – December). What dictates this seasonal variation in upwelling type?

5.1. The Pacific water – Atlantic water interface

Using the first year of SBI mooring array data (August 2002 – August 2003), Nikolopoulos et al. (2009) constructed a timeseries of the PW-AW interface depth and noted that it deepens in summer and shoals in late-fall (no other mention was made of it). In light of the seasonality in upwelling noted above, this motivates us to consider variations in the PW-AW interface depth more carefully. The idea is that the type of upwelling that occurs is dependent on how readily each of the water types is accessible seaward of the boundary current. As such, we need to investigate the signals in the PW-AW interface away from the region where the upwelling takes place.

The above results (Fig. 4) and previous studies indicate that the signature of upwelling is strong on the upper continental slope – in particular at the BS3 mooring site. Therefore, to look for seasonality in the PW-AW interface depth, we need to consider moorings that are farther into the basin, i.e. not directly influenced by the upwelling activity. We computed the monthly-averaged interface depth at the offshore SBI moorings (BS4 – BS7) for the time period September 2002 – August 2004 (Fig. 11a). All four timeseries vary in phase with each other and display a clear seasonal pattern, in line with that noted by Nikolopoulos et al. (2009). To shed further light

463 on this we also composited the PW-AW interface depth at each mooring site for the normalized
464 upwelling event (Fig. 11b, where it should be noted that there are just 48 events in the composite
465 because the full mooring array was deployed for only two years). This demonstrates that the
466 upwelling signal was evident at moorings BS4 and BS5, but that there was very little upwelling
467 signal at the two offshore-most sites BS6 and BS7 (there was a slight deflection of the interface of
468 approximately 5 m).

469 Therefore, we averaged the interface depth at BS6 and BS7 and took this as a measure of the
470 conditions offshore of the boundary current (BS6 failed in the second year, so only BS7 was used
471 then). Notably, when the interface depth was shallower than approximately 160 m, all of the
472 upwelling events during the two-year period were AW-type. Conversely, all of the PW-type
473 upwelling events occurred when the boundary was deeper than this (some AW events occurred
474 under this condition as well). This suggests that the interior interface depth plays a primary role in
475 determining whether AW versus PW is upwelled to the shelfbreak.

476 *5.2. Effect of wind stress curl*

477 What causes the seasonal change in the depth of the PW-AW interface? Atmospheric forcing
478 is an obvious candidate. Many observational and modeling studies have shown that the anti-
479 cyclonic wind stress curl in the Canada Basin drives Ekman transport that advects freshwater from
480 the boundary to the Beaufort Gyre (e.g. Proshutinsky et al., 2002; 2009). The convergence of this
481 transport in the interior then deepens the halocline. Seasonally, the Ekman pumping in the basin is
482 weaker in the summer and stronger in the remainder of the year (Yang, 2006), which in turn implies
483 that the PW-AW interface is deeper in the winter. This is the opposite of what is shown in Fig.
484 11a, which suggests that the behavior of the interface just seaward of the boundary current (at the
485 base of the continental slope) is different than in the center of the Beaufort Gyre.

To investigate this, we correlated the monthly mean interface depth calculated above at the two offshore mooring sites with the monthly wind stress curl field over the Beaufort Sea and the Canada Basin using the ASR product. The wind stress curl was averaged into 1°×1° bins to reduce noise, and the correlation coefficient determined between the PW-AW interface timeseries and the curl at each grid point. The spatial distribution of correlation (Fig. 12a) reveals a region of significant negative correlation in the shelfbreak/slope region of western Alaskan Beaufort Sea, where the mooring array was located, and a positive correlation farther to the northwest in the Canada Basin. This indicates that the situation is different in the interior basin versus the near-boundary region. Using the 13-year ASR record we then computed the correlation between the wind stress curl close to mooring BS7 and the wind stress curl at each data point in the domain (Fig. 12b). This shows a band of high-correlation along the slope of the western Alaskan Beaufort Sea in the vicinity of the mooring array. As such, we chose the area delimited by the box in Fig. 12 as the relevant region for averaging the wind stress curl.

The resulting monthly area-averaged wind stress curl for September 2002 – August 2004 shows good agreement (R= -0.63) with the monthly interface depth timeseries (Fig. 13): the interface becomes shallower when the wind stress curl increases, and vice versa. Note that the curl is negative during the summer months, so that there is Ekman pumping during the time period when the PW-AW interface is deepest and the PW upwelling events occur. This indicates that, while the wind stress curl does not drive the upwelling locally at the shelfbreak (Fig. 2b), offshore of the boundary the seasonal variation in curl impacts the accessibility of the AW to be drawn to the shelfbreak via the upwelling. We note that the changes in interface depth predicted by the wind stress curl ($h = t\nabla\times\tau/\rho_0 f$) only accounts for 36% of the observed monthly changes on average. This is discussed in Section 6.

509 *5.3. Atmospheric patterns*

510 We now return to the atmospheric fields to further clarify the seasonal variation of the wind
511 stress curl near the boundary. Using the ASR product, we constructed a latitude-time distribution
512 of climatological monthly mean wind stress curl over the period 2000 – 2013 in the vicinity of the
513 mooring array (Fig. 14). In the northern part of the domain the wind stress curl is negative
514 associated with the Beaufort High (see also Fig. 7). However, in the southern part of the domain,
515 including over the land (south of the dashed grey line), the curl is positive. One sees that the zero-
516 curl line is located south of the mooring array during the summer months and north of it remainder
517 of the year. This seasonal migration explains the timeseries of wind stress curl in Fig. 13.

518 What causes the latitudinal variation in the zero wind stress curl line? To answer this we
519 composited the SLP for the periods during 2000 – 2013 when the zero-curl line was north of its
520 mean latitude plus one standard deviation (25 months), and south of its mean latitude plus one
521 standard deviation (22 months). The former shows the Aleutian Low situated in the Gulf of Alaska
522 and the Beaufort High displaced to the west (Fig. 15a). This is similar to the winter SLP pattern
523 shown in Brugler et al. (2014) (17 of 25 months in the composite of Fig. 15a are in winter). By
524 contrast, the latter composite shows a well-developed Beaufort High with barely any signature of
525 the Aleutian Low (Fig. 15b), in agreement with the summertime SLP pattern from Brugler et al.
526 (2014) (20 of 22 months comprising Fig. 15b are in summer). Notably, the SLP composite when
527 the zero-curl line is located to the north is very close to that associated with the AW-type upwelling
528 (compare Figs. 7a and 15a), while the SLP composite when the zero-curl line is to the south reflects
529 the conditions when PW-type upwelling prevails (compare Figs. 7b and 15b). Hence we conclude
530 that the north-south migration of the zero-curl line associated with the behavior of the two

atmospheric centers of action dictates, to first order, the type of water that can be upwelled to the Beaufort shelfbreak.

6. Discussion

Our calculations indicate that, while the wind stress curl is highly correlated with PW-AW interface, the degree of deflection of the interface implied by the Ekman pumping/suction accounts for only a portion of the observed interface changes. It is important to keep in mind, however, that the spatial resolution of the ASR fields is 30 km, and if there were a higher resolution product then the curl signal would likely be significantly stronger. (Indeed, the ASR-derived curl is much larger than the curl computed using 80 km ERA-I reanalysis product.) Nonetheless, in light of the high positive correlation between the PW-AW interface at BS6–7 and the curl in the Canada Basin (Fig. 12a), there could also be a remote effect. In particular, the seasonal adiabatic migration of the pycnocline in Canada Basin could be compensated by an oppositely phased migration near the boundary in order to conserve volume (Proshutinsky, 1988). By assuming the Arctic Ocean has two layers in the vertical, Proshutinsky and Johnson (1997) found that, in response to wind forcing, the interface is raised in the center of the Arctic while it is depressed along the coasts, and vice versa. We also note that ice is not considered in this study, which may lead to an underestimate of the interface movement. As discussed in the introduction, mobile pack ice is able to enhance the surface stress on the sea surface (Häkkinen, 1986; Schulze and Pickart, 2012), which in turn could lead to stronger values of the wind stress curl and larger isopycnal displacements.

Another possibility for varying the interface height seaward of the boundary is steric changes to the water column. Such steric-driven pycnocline depth fluctuations are reflected in the varying sea level which has been well studied (e.g. McGregor et al., 2012; Palanisamy et al., 2015). Both

currents and atmospheric systems make a signification contribution to the heat and freshwater fluxes within our study region. The shelfbreak jet transports a significant amount of freshwater and heat to the vicinity of the mooring, particularly in summer (Brugler et al., 2014). As demonstrated by von Appen and Pickart (2012), the summertime structure of the jet is baroclinically unstable and hence is likely to shed eddies of Pacific water offshore (e.g. Spall et al., 2008). With regard to atmospheric forcing, even a single storm can flux a significant amount of heat and freshwater from the shelf to the interior (Pickart et al., 2013b). Consequently, we can expect an enhanced presence of relatively warm and fresh Pacific summer water in the Alaskan Beaufort Sea during the summer months which would in turn depress the pycnocline downward.

Previous studies, as well as the results presented here, have demonstrated that the Beaufort shelfbreak jet is highly sensitive to the wind (e.g. Nikolopoulos et al., 2009; Pickart et al., 2009; Brugler et al., 2014). To further assess the effect of wind on the jet, we considered a wind strength index, $W_s = u_{wind}/u_{buoy}$, where u_{wind} and u_{buoy} are the wind-driven and buoyancy-driven velocity scales, respectively (Whitney and Garvine, 2005; Sutherland and Pickart, 2008). In particular, $u_{wind} = \sqrt{\frac{\rho_{air}}{\rho}\frac{C_{10}}{C_D}}U_{wind}$ and $u_{buoy} = \frac{\sqrt{g'h}}{K}$, where ρ_{air} (ρ) is the air (water) density, C_{10} (C_D) is the surface (bottom) drag coefficient, U_{wind} is the wind speed, $\sqrt{g'h}$ is the internal wave speed, K is the dimensionless current width. $|W_s| > 1$ indicates that the wind plays an essential role in the existence of the current (e.g. $|W_s| = 4.0$ in Scottish Coastal Current), while $|W_s| < 1$ suggests that buoyancy forcing is dominant (e.g. $|W_s| = 0.1$ for the Alaskan Coastal Current) (Whitney and Garvine, 2005). Using all six years of data, we calculate a $|W_s|$ of ~0.3, implying that the Beaufort shelfbreak jet is not predominantly a wind-driven feature. This is in line with the results of Lin et al. (2016) who determined that the wind-driven component of the shelfbreak jet does not account for the dominant seasonal variation in total transport. During upwelling events,

577 however, the shelfbreak jet is readily reversed by easterly winds and under these conditions $|W_s| >$
578 1. This is similar to the coastal current in the South Atlantic Bight for which $|W_s| = 0.6$ on average,
579 but during upwelling events it increases to 1.7 (Whitney and Garvine, 2005). One should keep in
580 mind that, in summer, the Beaufort shelfbreak jet is the extension of the Alaskan Coastal Current
581 which is predominantly buoyancy-driven (Royer, 1983). Overall, the value of W_s computed here
582 suggests that, while not primarily wind-driven, the Beaufort shelfbreak jet is easily modified by
583 the wind.

584 As mentioned in the introduction, our study site corresponds to the DBO-6 line, which is one
585 of the areas that has been identified for targeted biological measurements in the Pacific Arctic by
586 the DBO program. Therefore, the results presented here offer some insights with regard to
587 ecosystem studies being carried out within the DBO framework. Upwelling and the associated
588 cross-slope circulation along the Beaufort slope have been shown to significantly impact the fluxes
589 of heat and freshwater into the basin as well as the flux of nitrate onto the shelf (Pickart et al.,
590 2013b). In addition, zooplankton can be upwelled to the shelf influencing the feeding behavior of
591 bowhead whales (Bradstreet et al., 1987; Okkonen et al. 2011) as well as gray whales (Pickart et
592 al., this issue). The fall migration of bowheads and belugas along the Beaufort slope has been
593 shown to coincide with the autumn peak in shelfbreak upwelling (Lin et al, 2016). In addition to
594 quantifying various aspects of upwelling in this region, our results demonstrate that the basin water
595 accessible for upwelling varies over the course of the year due to the large scale atmospheric
596 circulation. This in turn will affect the biologically important fluxes that occur in this region. The
597 same may also be true of Barrow Canyon – where the DBO-5 line is located – which is another
598 place subject to frequent upwelling of Pacific and Atlantic waters (Carmack and Kulikov, 1998;
599 Okkonen et al., 2009; Watanabe, 2011; Pisareva et al., this issue).

7. Summary

Using 6 years of mooring data, together with weather station data and atmospheric reanalysis fields, we have clarified the driving factors and general characteristics of upwelling on the Alaskan Beaufort Sea slope. Wind-driven upwelling occurs when the near-bottom potential density anomaly (relative to the climatological monthly mean) at the mooring in the center of the shelfbreak jet is positive, during times of easterly (alongcoast) wind. While there is a strong correlation between the upwelling and the cumulative Ekman transport, there is no such relationship involving the local wind stress curl, implying that this process is due to coastal upwelling.

We composited all 115 upwelling events over the 6-year record by normalizing the time period of each event from 0 – 1. The canonical upwelling event unfolds as follows: As the easterly wind intensifies, the shelfbreak jet weakens and reverses to the west in the surface layer. Shortly after this the upwelling commences and the wind reaches its peak, reversing the shelfbreak jet from top to bottom. At the end of the event a bottom-intensified, eastward-flowing "rebound jet" is established that is stronger than the normal shelfbreak jet. The cross-isobath circulation displays a three-layer structure with onshore flow in the surface layer, offshore flow in the middle of the water column, and onshore flow near the bottom. This structure arises because the orientation of the reversed shelfbreak jet is slightly onshore which overwhelms the cross-isobath surface Ekman transport. The vertically-integrated along-isobath momentum balance supports this interpretation and indicates that the rebound jet is driven by the zonal gradient in sea surface height.

During roughly two thirds of the events, Atlantic water (AW) is upwelled to the shelfbreak, whereas for the remaining events only Pacific water (PW) is upwelled. During the PW-type events

623 the hydrographic response is more muted and both the primary and secondary circulation is weaker.
624 Notably, the easterly wind strength is, on average, the same for both types of events. Furthermore,
625 most of the PW events occur during summer, while the majority of the AW events occur during
626 the remainder of the year (with a peak in spring and fall). We have argued that the primary factor
627 dictating the type of upwelling event is the seasonal variation in the PW-AW interface depth
628 seaward of the shelfbreak. For the two-year period in which we had data offshore, when the
629 interface was shallower than about 160 m all of the events were AW-type, whereas all of the PW-
630 type events occurred when the interface was deeper than this.
631 Using the reanalysis fields, we determined that the wind stress curl near the boundary is
632 strongly linked to the variation in PW-AW interface depth. In particular, negative wind stress curl
633 pumps the interface down during summer, and positive curl lifts it in winter. This happens because
634 the zero wind stress curl line migrates across the Beaufort slope seasonally. Compositing the times
635 when the line is to the north reveals a clear atmospheric pattern, with a deep Aleutian low in the
636 Gulf of Alaska and a Beaufort High displaced to the west. Conversely, when the zero curl line is
637 to the south, there is a well-developed Beaufort High with virtually no signature of the Aleutian
638 Low. These patterns agree with the seasonal composites of Brugler et al. (2014). Hence, the two
639 atmospheric centers of action – the Beaufort High and the Aleutian Low – control the annual
640 variation of local wind stress curl, which in turn alters the PW-AW interface depth and dictates
641 the type of upwelling that occurs on the Beaufort slope. Any future changes in the storm climate
642 of the region may therefore have direct bearing on the shelf-basin exchange of physical and
643 biological properties by altering the halocline and nutricline depth offshore of the boundary.
644
645

Acknowledgements

The authors would like to thank D. Torres and F. Bahr for processing the mooring data, C. Nobre for providing technical support, and D. Bromwich for access to the ASR data. PL and JH received support from the National Basic Research Program of China (2015CB954004) and the China Scholarship Council. RP and MS were supported by the National Science Foundation Office of Polar Programs under grants PLR-1504333 and PLR-1415489, respectively. KM was funded by the Natural Sciences and Engineering Research Council of Canada.

References

Aagaard, K., 1984. The Beaufort Undercurrent, in The Alaskan Beaufort Sea, edited by Barnes P.W., Schell D.M., Reimnitz, E., pp. 47–71, Academic, San Diego, Calif.

Aksenov, Y., Ivanov, V.V., Nurser, A., Bacon, S., Polyakov, I.V., Coward, A.C., Naveira-Garabato, A.C., Beszczynska-Moeller, A., 2011. The Arctic circumpolar boundary current. J. Geophys. Res. Oceans, 116, C09017, doi:10.1029/2010JC006637.

Bradstreet, M., Fissel., D.B., Moen, J., 1987. Water mass distributions in the Canadian Beaufort Sea. Oceans '87: The Ocean -- An International Workplace, Halifax, N.S.(Canada), 28 Sep–1 Oct 1987.

Bromwich, D.H., Wilson, A.B., Bai, L.-S., Moore, G.W., Bauer, P., 2015. A comparison of the regional Arctic System Reanalysis and the global ERA-Interim Reanalysis for the Arctic. Q.J.R. Meteorol. Soc., 10, 1002. DOI:10.1002/qj.2527.

Brugler, E.T., Pickart, R.S., Moore, G.W.K., Roberts, S., Weingartner, T.J., Statscewich, H., 2014. Seasonal to interannual variability of the Pacific water boundary current in the Beaufort Sea. Prog. Oceanogr. 127, 1–20.

669 Carmack, E.C., Kulikov, E.A., 1998. Wind-forced upwelling and internal Kelvin wave generation
670 in Mackenzie Canyon, Beaufort Sea, J. Geophys. Res., 103, 18,447–18,458.
671 Favorite, F., 1976. Oceanography of the subarctic Pacific region, 1960–1971. Bull. Int. North Pac.
672 Commission, 31, 1960–1971.
673 Fratantoni, P.S., Zimmermann S., Pickart R.S., Swartz M., 2006. Western Arctic Shelf- basin
674 Interaction Experiment: Processing and cali- bration of moored profiler data form the
675 Beaufort shelf-edge mooring array, Woods Hole Oceanogr. Inst. Tech. Rep. WHOI-2006-15,
676 34 pp., Woods Hole Oceanogr. Inst., Woods Hole, Mass.
677 Gong, D., Pickart, R.S., 2016. Early Summer Water Mass Transformation in the Eastern Chukchi
678 Sea. Deep Sea Res., Part II, 130, 43–55.
679 Häkkinen, S., 1986. Coupled ice-ocean dynamics in the marginal ice zones:
680 Upwelling/downwelling and eddy generation. J. Geophys. Res. Oceans, 91, 819–832.
681 Hufford, G.L., 1974. On apparent upwelling in the southern Beaufort Sea. J. Geophys. Res., 79,
682 1305–1306.
683 Huyer, A., Sobey, E., Smith, R.L., 1979. The spring transition in currents over the Oregon
684 continental shelf. J. Geophys. Res., 84, 6995–7011.
685 Itoh, M., Shimada, K., Kamoshida, T., McLaughlin, F., Carmack, E., Nishino, S., 2012.
686 Interannual variability of Pacific Winter Water inflow through Barrow Canyon from 2000 to
687 2006. J. Oceanogr., 68, 575–592.
688 Karcher, M., Kauker, F., Gerdes, R., Hunke, E., Zhang, J., 2007. On the dynamics of Atlantic
689 Water circulation in the Arctic Ocean. J. Geophys. Res. Oceans, 112, C04S02.
690 Lin, P., Pickart, R.S., Stafford, K.M., Moore, G.W.K., Torres, D.J., Bahr, F., Hu, J., 2016, Seasonal
691 variation of the Beaufort shelfbreak jet and its relationship to Arctic cetacean occurrence. J.

692 Geophys. Res. Oceans. 121, doi:10.1002/2016JC011890.
693 Lowry, K.E., Pickart, R.S., Mills, M.M., Brown, Z.W., van Dijken, G.L., Bates, N.R., Arrigo, K.R.,
694 2015. The influence of winter water on phytoplankton blooms in the Chukchi Sea. Deep Sea
695 Res., Part II, 118, 53–72.
696 Macdonald, R.W., Anderson, L.G., Christensen, J.P., Miller, L.A., Semiletov, I.P., Stein, R., 2010.
697 Polar margins: the Arctic Ocean. In: Liu, K.K., et al. (Eds.), Carbon and Nutrient Fluxes in
698 Continental Margins: A Global Synthesis. Springer, New York, pp. 291–303.
699 Martin, T., Steele, M., Zhang, J., 2014. Seasonality and long-term trend of Arctic Ocean surface
700 stress in a model. J. Geophys. Res. Oceans, 119, 1723–1738.
701 McGregor, S., Gupta, A.S., England, M.H., 2012. Constraining wind stress products with sea
702 surface height observations and implications for Pacific Ocean sea level trend attribution. J.
703 Climate, 25(23), 8164-8176.
704 Moore, G.W.K., Bromwich, D.H., Wilson, A.B., Renfrew, I., Bai, L., 2016. Arctic System
705 Reanalysis improvements in topographically forced winds near Greenland. Q.J.R. Meteorol.
706 Soc., 142: 2033–2045. doi:10.1002/qj.2798.
707 Moore, S., Grebmeier, J.M., same issue. The Distributed Biological Observatory: Linking Physics
708 to Biology in the Pacific Arctic Region.
709 Nikolopoulos, A., Pickart, R.S., Fratantoni, P.S., Shimada, K., Torres, D.J., Jones, E.P., 2009. The
710 western Arctic boundary current at 152°W: Structure, variability, and transport. Deep Sea
711 Res., Part II, 56, 1164–1181.
712 Okkonen, S.R., Ashjian, C., Campbell, R.G., Clarke, J., Moore, S.E., Taylor K., 2011. Satellite
713 observations of circulation features associated with a bowhead whale feeding ‘‘hotspot’’ near
714 Barrow, Alaska, Remote Sens. Environ., 115, 2168–2174.

715 Okkonen, S.R., Ashjian, C.J., Campbell, R.G., Maslowski, W., Clement-Kinney, J.L., Potter, R.,
716 2009. Intrusion of warm Bering/Chukchi waters onto the shelf in the western Beaufort Sea, J.
717 Geophys. Res., 114, C00A11, doi:10.1029/2008JC004870.
718 Palanisamy, H., Cazenave, A., Delcroix, T., Meyssignac, B., 2015. Spatial trend patterns in the
719 Pacific Ocean sea level during the altimetry era: the contribution of thermocline depth change
720 and internal climate variability. Ocean Dynamics, 65(3), 341-356.
721 Pickart, R.S., Moore, G., Mao, C., Bahr, F., Nobre, C., Weingartner, T.J., 2016. Circulation of
722 winter water on the Chukchi shelf in early Summer. Deep Sea Res., Part II, 130, 56–75.
723 Pickart, R.S., Moore, G.W.K., Torres, D.J., Fratantoni, P.S., Goldsmith, R.A., Yang, J., 2009.
724 Upwelling on the continental slope of the Alaskan Beaufort Sea: Storms, ice, and
725 oceanographic response. J. Geophys. Res., 114, C00A13, doi:10.1029/2008JC005009.
726 Pickart, R.S., Schulze, L.M., Moore, G.W.K., Charette, M.A., Arrigo, K.R., van Dijken, G.,
727 Danielson, S.L., 2013a. Long-term trends of upwelling and impacts on primary productivity
728 in the Alaskan Beaufort Sea. Deep Sea Res., Part I, 79, 106–121.
729 Pickart, R.S., Spall, M.A., Mathis, J.T., 2013b. Dynamics of upwelling in the Alaskan Beaufort
730 Sea and associated shelf-basin fluxes. Deep Sea Res., Part I, 76, 35–51.
731 Pickart, R.S., Spall, M.A., Moore, G.W.K., Weingartner, T.J., Woodgate, R.A., Aagaard, K.,
732 Shimada, K., 2011. Upwelling in the Alaskan Beaufort Sea: Atmospheric forcing and local
733 versus non-local response. Prog. Oceanogr., 88, 78–100.
734 Pickart, R.S., Torres, D.J., Ashjian, C.J., Moore, S.E., same issue. Autumn upwelling in the
735 Alaskan Beaufort Sea influences gray whale call occurrence.
736 Pisareva, M.N., Pickart, R.S., Fratantoni, P.S., Weingartner, T.J., same issue. On the nature of
737 wind-forced upwelling in Barrow Canyon.

738 Pisareva, M.N., Pickart, R.S., Spall, M., Nobre, C., Torres, D., Moore, G., Whitledge, T.E., 2015.
739 Flow of Pacific water in the western Chukchi Sea: Results from the 2009 RUSALCA
740 expedition. Deep Sea Res., Part I, 105, 53–73.
741 Pringle, J.M., 2002. Enhancement of Wind-Driven Upwelling and Downwelling by Alongshore
742 Bathymetric Variability. J. Phys. Oceanogr., 32, 3101–3112.
743 Proshutinsky, A.Y., 1988. Modeling seasonal fluctuations of the level of the Arctic Ocean, Sov.
744 Meteorol. Hydrol., Engl. Transl., 2, 57–65.
745 Proshutinsky, A., Bourke, R., McLaughlin, F., 2002. The role of the Beaufort Gyre in Arctic
746 climate variability: Seasonal to decadal climate scales. Geophys. Res. Lett., 29 (23), 2100,
747 doi:10.1029/2002GL015847.
748 Proshutinsky, A., Krishfield, R., Timmermans, M.L., Toole, J., Carmack, E., McLaughlin, F.,
749 Williams, W.J., Zimmermann, S., Itoh, M., Shimada, K., 2009. Beaufort Gyre freshwater
750 reservoir: State and variability from observations. J. Geophys. Res. Oceans, 114, C00A10,
751 doi:10.1029/2008JC005104.
752 Proshutinsky, A.Y., Johnson M.A., 1997. Two circulation regimes of the wind-driven Arctic
753 Ocean, J. Geophys. Res., 102(C6), 12493–12514, doi:10.1029/97JC00738.
754 Reed, R.J., Kunkel, B.A., 1960. The Arctic circulation in summer. J. Meteor., 17, 489–506.
755 Røed, L.P., O'Brien, J.J., 1983. A coupled ice-ocean model of upwelling in the marginal ice zone.
756 J. Geophys. Res. Oceans, 88, 2863–2872.
757 Royer, T.C., 1983. Observations of the Alaska Coastal Current, in Coastal Oceanography. In Gade,
758 H., Edwards, A., Svendsen, H. (Eds), Plenum, New York, pp. 9 – 30.
759 Rudels, B., Jones, E.P., Schauer, U., Eriksson, P., 2004. Atlantic sources of the Arctic Ocean
760 surface and halocline waters. Polar Res. 23, 181–208.

761 Schulze, L.M., Pickart, R.S., 2012. Seasonal variation of upwelling in the Alaskan Beaufort Sea:
762 Impact of sea ice cover. J. Geophys. Res. Oceans, 117, C06022, doi:10.1029/2012JC007985.
763 Spall, M.A., Pickart, R.S., Fratantoni, P.S., Plueddemann, A.J., 2008. Western Arctic shelfbreak
764 eddies: Formation and transport. J. Phys. Oceanogr., 38, 1644–1668.
765 Sutherland, D.A., Pickart, R.S., 2008. The East Greenland coastal current: Structure, variability,
766 and forcing. Prog. Oceanogr., 78(1), 58–77.
767 von Appen, W., Pickart, R.S., 2012. Two configurations of the western Arctic shelfbreak current
768 in summer. J. Phys. Oceanogr., 42, 329–351.
769 Walsh, J.E., 1978. Temporal and spatial scales of the Arctic circulation. Monthly Weather Review,
770 106, 1532–1544.
771 Watanabe, E., 2011. Beaufort shelf break eddies and shelf-basin exchange of Pacific summer water
772 in the western Arctic Ocean detected by satellite and modeling analyses, J. Geophys. Res.,
773 116, C08034, doi:10.1029/ 2010JC006259.
774 Watanabe, E., 2013. Linkages among halocline variability, shelf-basin interaction, and wind
775 regimes in the Beaufort Sea demonstrated in pan-Arctic Ocean modeling framework. Ocean
776 Modell., 71, 43–53.
777 Weingartner, T.J., Potter, R.A., Stoudt, C.A., Dobbins, E.L., Statscewich, H., Winsor, P.R.,
778 Mudge, T.D., Borg, K., 2017. Transport and thermohaline variability in Barrow Canyon on
779 the Northeastern Chukchi Sea Shelf. J. Geophys. Res. Oceans, 122, doi:10.1002/
780 2016JC012636.
781 Whitney, M.M., Garvine, R.W., 2005. Wind influence on a coastal buoyant outflow. J. Geophys.
782 Res., 110, C03014, doi:10.1029/2003JC002261.
783 Wilson, J.G., Overland, J.E., 1986. Meteorology. In: Hood, D.W., Zimmermann, S.T. (Eds.), The

Gulf of Alaska, Physical Environment and Biological Resources. Alaska Office, Ocean Assessments Division, National Oceanic and Atmospheric Administration, US Department of Commerce, pp. 31–54.

Yang, J., 2006. The Seasonal Variability of the Arctic Ocean Ekman Transport and Its Role in the Mixed Layer Heat and Salt Fluxes. J. Clim., 19, 5366–5387.

Zhang, X., Walsh, J.E., Zhang, J., Bhatt, U.S., Ikeda, M., 2004. Climatology and interannual variability of Arctic cyclone activity: 1948–2002. J. Clim., 17, 2300–2317.

807 **Captions**

808 **Fig. 1.** Locations of the moorings (black circles) used in the study and the schematic circulation
809 of the region. Mooring BS3 (blue star) was deployed for 6 years, the others deployed for 2 years.
810 The green arrow denotes the Alaskan Coastal Current and Beaufort shelfbreak jet. The blue arrows
811 are the schematic Pacific water pathways on the northeast Chukchi shelf. The meteorological data
812 used in the study come from the weather station at Barrow, AK. The bathymetric contours are in
813 meters.

814

815 **Fig. 2.** (a) The value of the upwelling index versus cumulative Ekman transport for AW-type
816 upwelling events (red dots) and PW-type upwelling events (blue dots). The lines of best fit for
817 AW-type events (red line), PW-type events (blue line), and all events (black line) with its 95%
818 confidence level (black dashed line) are shown. (b) Upwelling index versus local wind stress curl
819 for all of the upwelling events. The standard errors are included.

820

821 **Fig. 3.** Composite upwelling event constructed from the 115 individual events. (a) The alongcoast
822 windspeed (m s^{-1}) where negative is easterly; (b) The potential density anomaly (kg m^{-3}). The
823 shading represents the standard error.

824

825 **Fig. 4.** Composite upwelling event constructed from the 115 individual events. (a) Potential
826 temperature (°C), (b) salinity, and (c) buoyancy frequency (color, N^2 (s^{-2})) overlain by potential
827 density (contours, kg m^{-3}). The PW-AW interface is denoted by thick lines.

828

Fig. 5. Composite upwelling event constructed from the 115 individual events. (a) Depth-averaged along-isobath velocity (positive is eastward). The shading represents the standard error. (b) Depth-dependent along-isobath velocity. (c) Depth-averaged cross-isobath velocity (positive is offshore). (d) Depth-dependent cross-isobath velocity. The 0 contours are highlighted. The units are m s^{-1}.

Fig. 6. Terms of the depth-integrated along-isobath momentum equation for the composite upwelling event: local acceleration (red); Coriolis force (black); wind stress (blue); bottom stress (yellow); cross-isobath divergence of momentum flux (DMF, dashed black); and pressure gradient force (PGF, green), which is computed as the residual.

Fig. 7. Composite sea level pressure (mb) and 10 m wind (vectors, m s^{-1}) from ASR for (a) the AW-type upwelling, and (b) the PW-type upwelling. The red star denotes the location of the BS3 mooring. BH = Beaufort High; AL = Aleutian Low.

Fig. 8. Composite upwelling event constructed from the 85 individual AW-type upwelling events from 2002 – 2004. (a) Salinity (color) overlaid by potential density (contours, kg m^{-3}). The thick lines indicate the PW-AW interface. (b) Along-isobath velocity (positive is eastward). (c) Cross-isobath velocity (positive is offshore). The 0 contours are highlighted.

Fig. 9. Same as Fig. 8. except for the 30 PW-type upwelling events.

Fig. 10. Seasonal variation of the occurrence of AW-type upwelling events (solid line) and PW-type upwelling events (dashed line).

Fig. 11. (a) Timeseries of monthly-averaged PW-AW interface depth for the four offshore SBI moorings (2002 – 2004). The standard errors are indicated. (b) Interface depth for the composite upwelling event constructed using the SBI data, for each of the four moorings.

Fig. 12. Spatial distribution of correlation coefficient (points with confidence level < 95% are not plotted). (a) Wind stress curl at each point versus the PW-AW interface depth; (b) Wind stress curl at each point versus the wind stress curl close to mooring BS7. The dashed box delimits the region over which the wind stress curl was averaged for the calculations in the text. The black stars denote the mooring locations.

Fig. 13. Timeseries of monthly-averaged PW-AW interface depth (m, blue) and monthly area-averaged wind stress curl ($\times 10^{-6}$ N m^{-3}, red) for September 2002 – August 2004. The standard errors are included.

Fig. 14. Latitude-time distribution of the climatological monthly mean wind stress curl ($\times 10^{-6}$ N m^{-3}) close to 152° W for the time period 2000 – 2013. The zero-curl contour with standard error (blue bars) is highlighted. The grey dashed line marks the location of coastline, and the grey dots are ASR data points. Black dots denote the mooring locations.

Fig. 15. Composite sea level pressure (mb) for the months when (a) the latitude of zero wind stress curl line is higher than the mean latitude plus one standard deviation, and (b) the latitude of zero wind stress curl line is lower than the mean latitude minus one standard deviation.

Figures

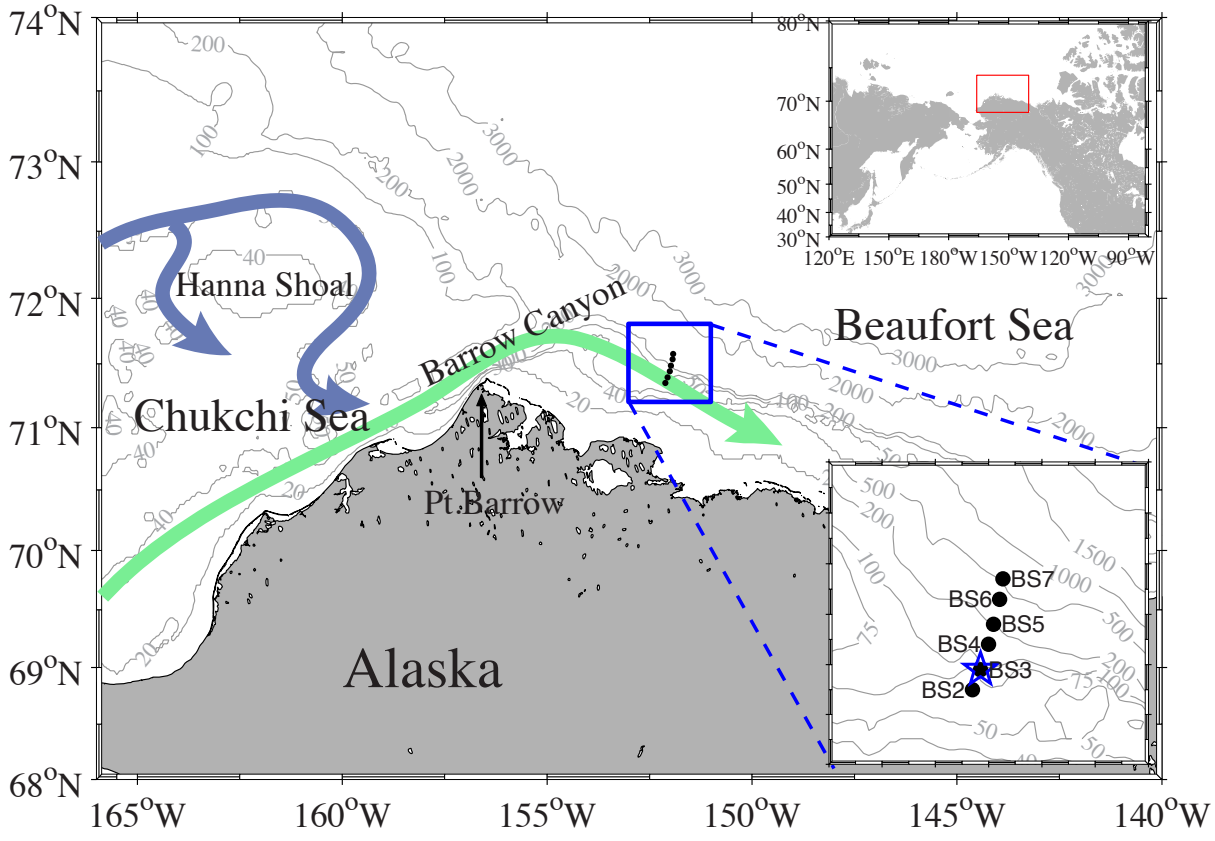

Fig. 1. Locations of the moorings (black circles) used in the study and the schematic circulation of the region. Mooring BS3 (blue star) was deployed for 6 years, the others deployed for 2 years. The green arrow denotes the Alaskan Coastal Current and Beaufort shelfbreak jet. The blue arrows are the schematic Pacific water pathways on the northeast Chukchi shelf. The meteorological data used in the study come from the weather station at Barrow, AK. The bathymetric contours are in meters.

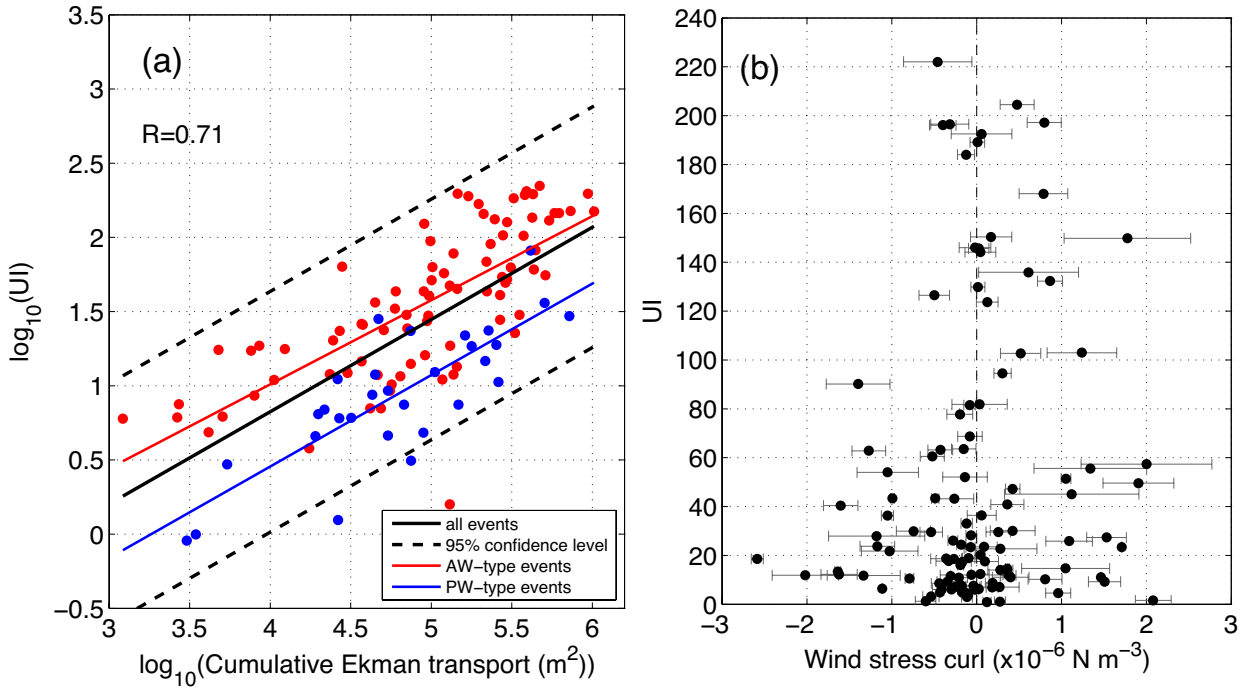

885

886 **Fig. 2.** (a) The value of the upwelling index versus cumulative Ekman transport for AW-type
887 upwelling events (red dots) and PW-type upwelling events (blue dots). The lines of best fit for
888 AW-type events (red line), PW-type events (blue line), and all events (black line) with its 95%
889 confidence level (black dashed line) are shown. (b) Upwelling index versus local wind stress curl
890 for all of the upwelling events. The standard errors are included.

891

892

893

894

895

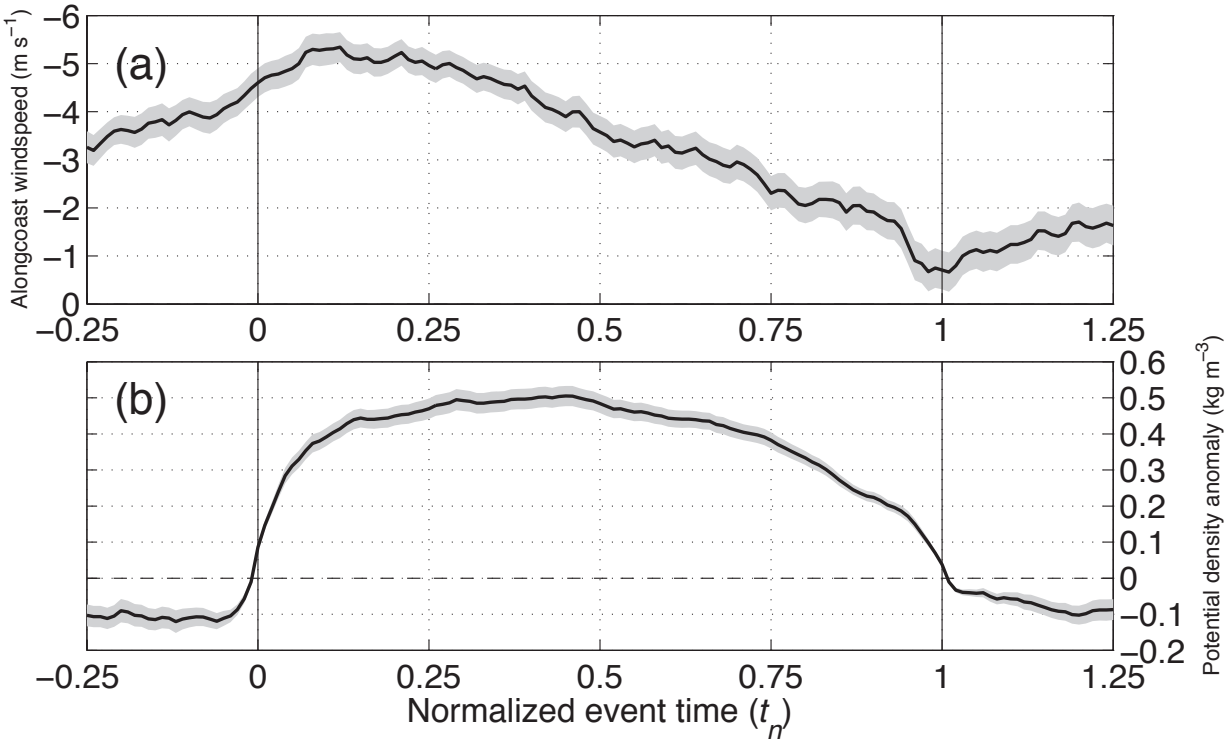

Fig. 3. Composite upwelling event constructed from the 115 individual events. (a) The alongcoast windspeed (m s^{-1}) where negative is easterly; (b) The potential density anomaly (kg m^{-3}). The shading represents the standard error.

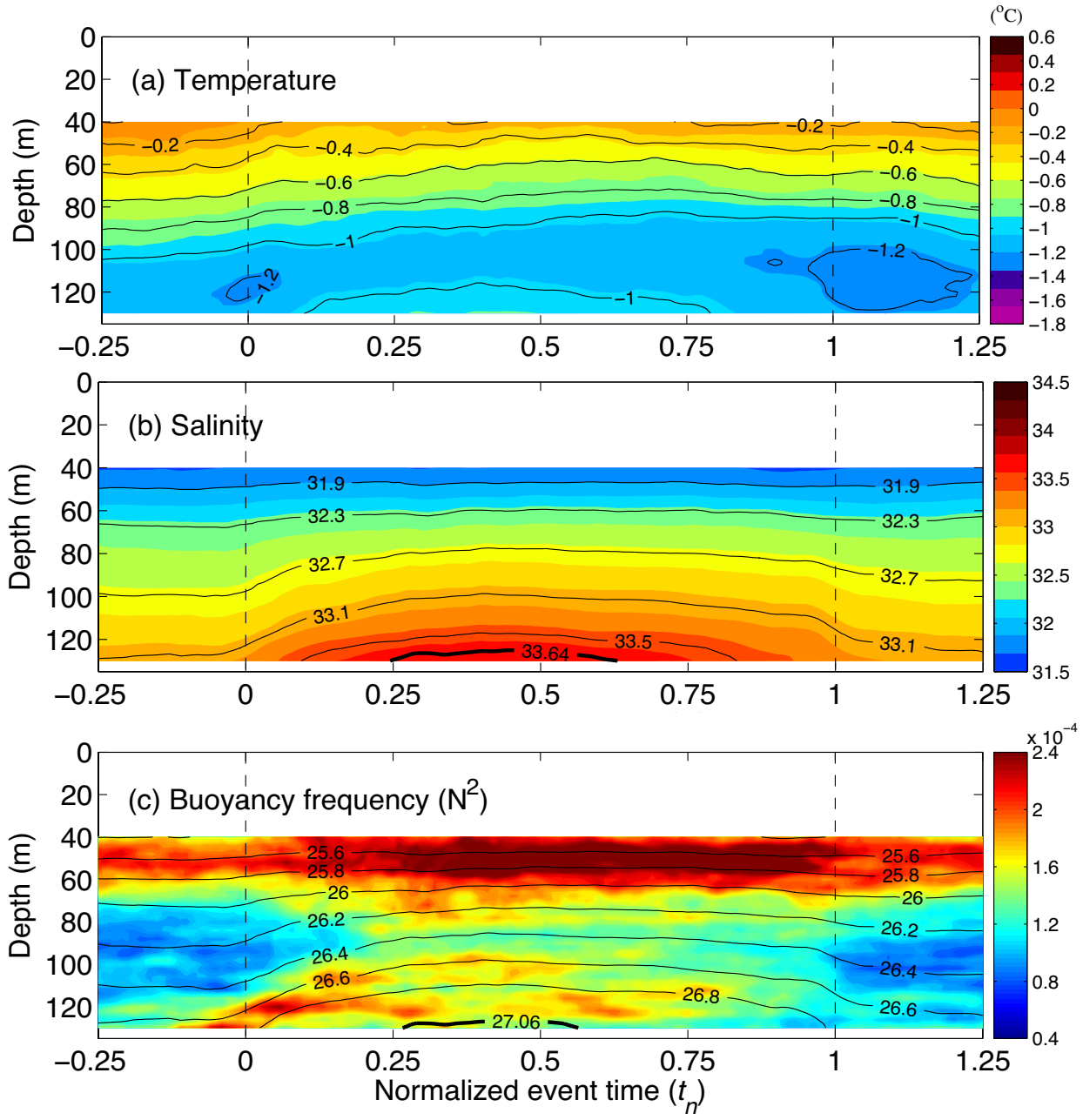

910

911 **Fig. 4.** Composite upwelling event constructed from the 115 individual events. (a) Potential

912 temperature (°C), (b) salinity, and (c) buoyancy frequency (color, N^2 (s^{-2})) overlain by potential

913 density (contours, kg m^{-3}). The PW-AW interface is denoted by thick lines.

914

915

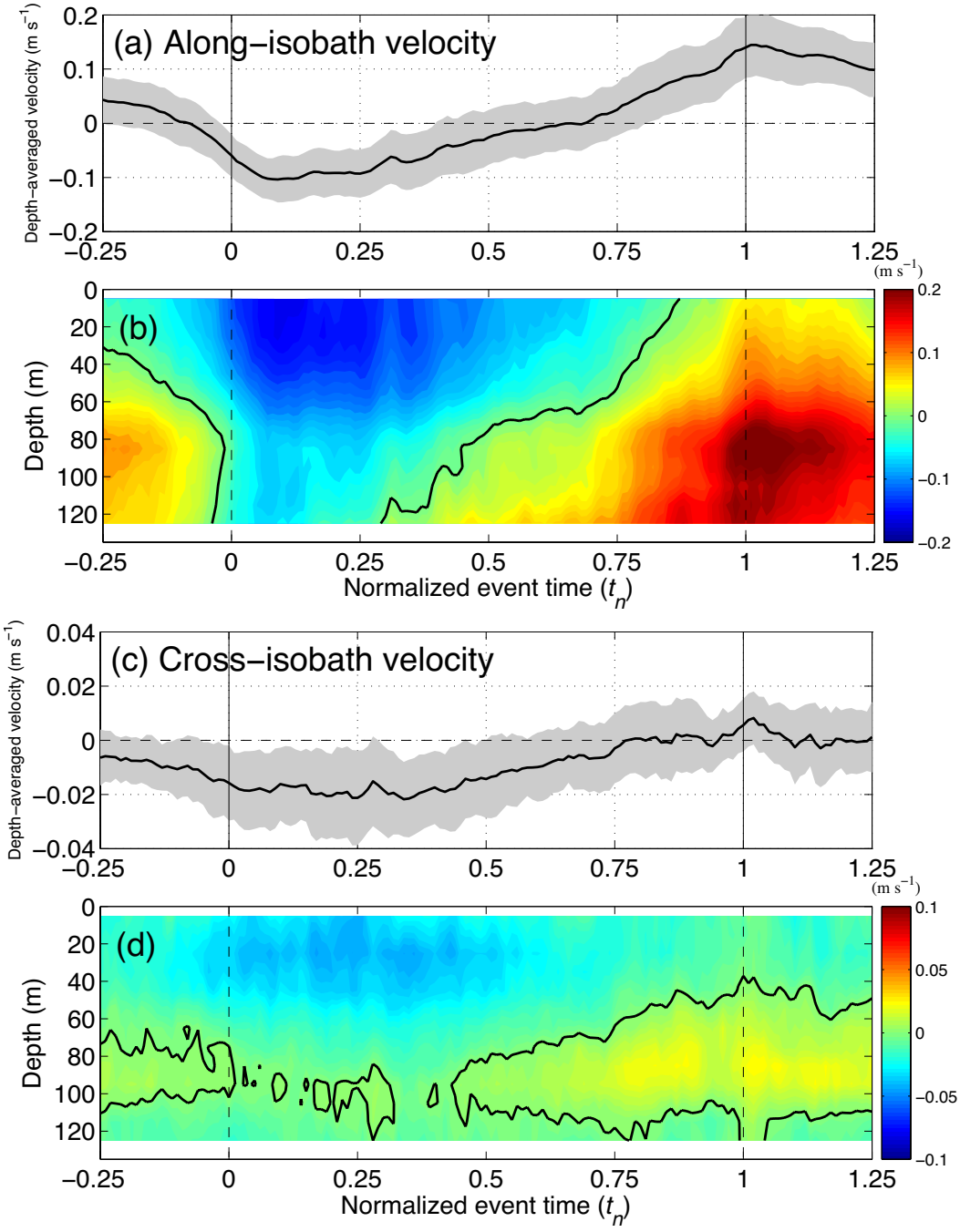

916

917 **Fig. 5.** Composite upwelling event constructed from the 115 individual events. (a) Depth-averaged
918 along-isobath velocity (positive is eastward). The shading represents the standard error. (b) Depth-
919 dependent along-isobath velocity. (c) Depth-averaged cross-isobath velocity (positive is offshore).
920 (d) Depth-dependent cross-isobath velocity. The 0 contours are highlighted. The units are m s^{-1}.

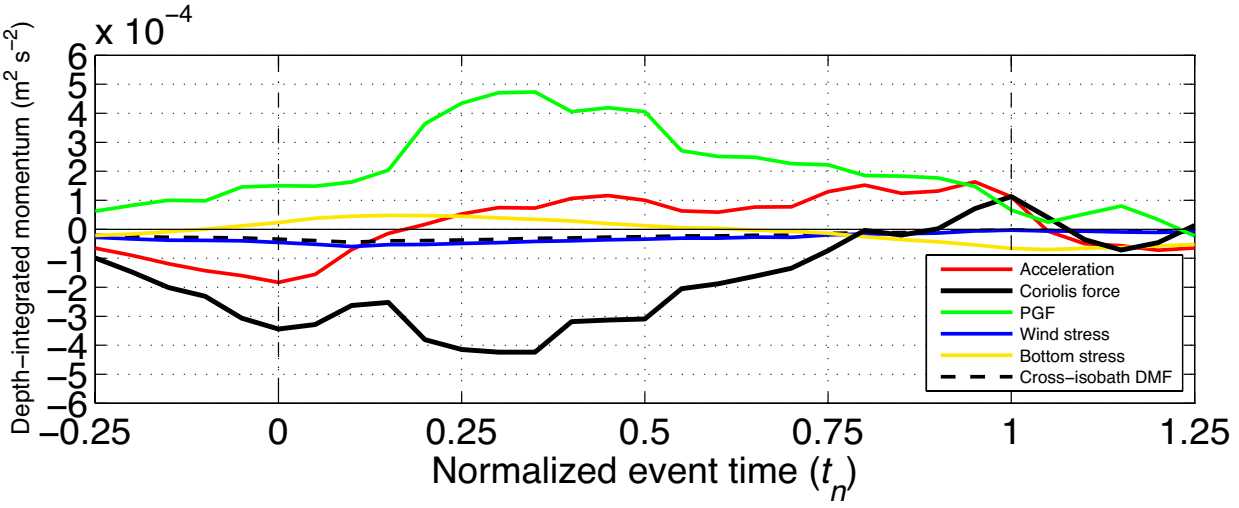

Fig. 6. Terms of the depth-integrated along-isobath momentum equation for the composite upwelling event: local acceleration (red); Coriolis force (black); wind stress (blue); bottom stress (yellow); cross-isobath divergence of momentum flux (DMF, dashed black); and pressure gradient force (PGF, green), which is computed as the residual.

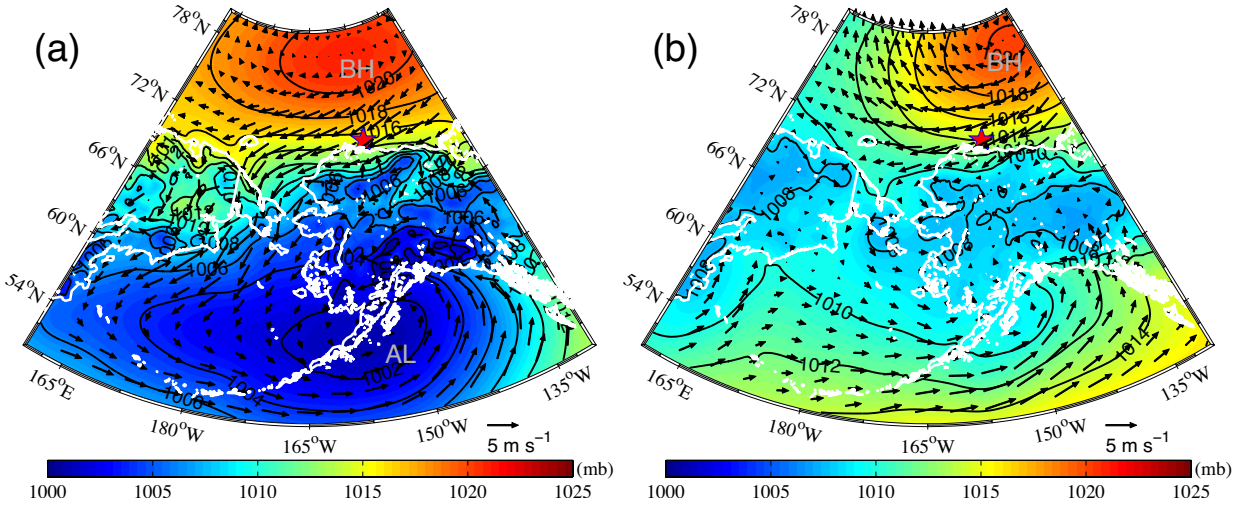

Fig. 7. Composite sea level pressure (mb) and 10 m wind (vectors, m s^{-1}) from ASR for (a) the AW-type upwelling, and (b) the PW-type upwelling. The red star denotes the location of the BS3 mooring. BH = Beaufort High; AL = Aleutian Low.

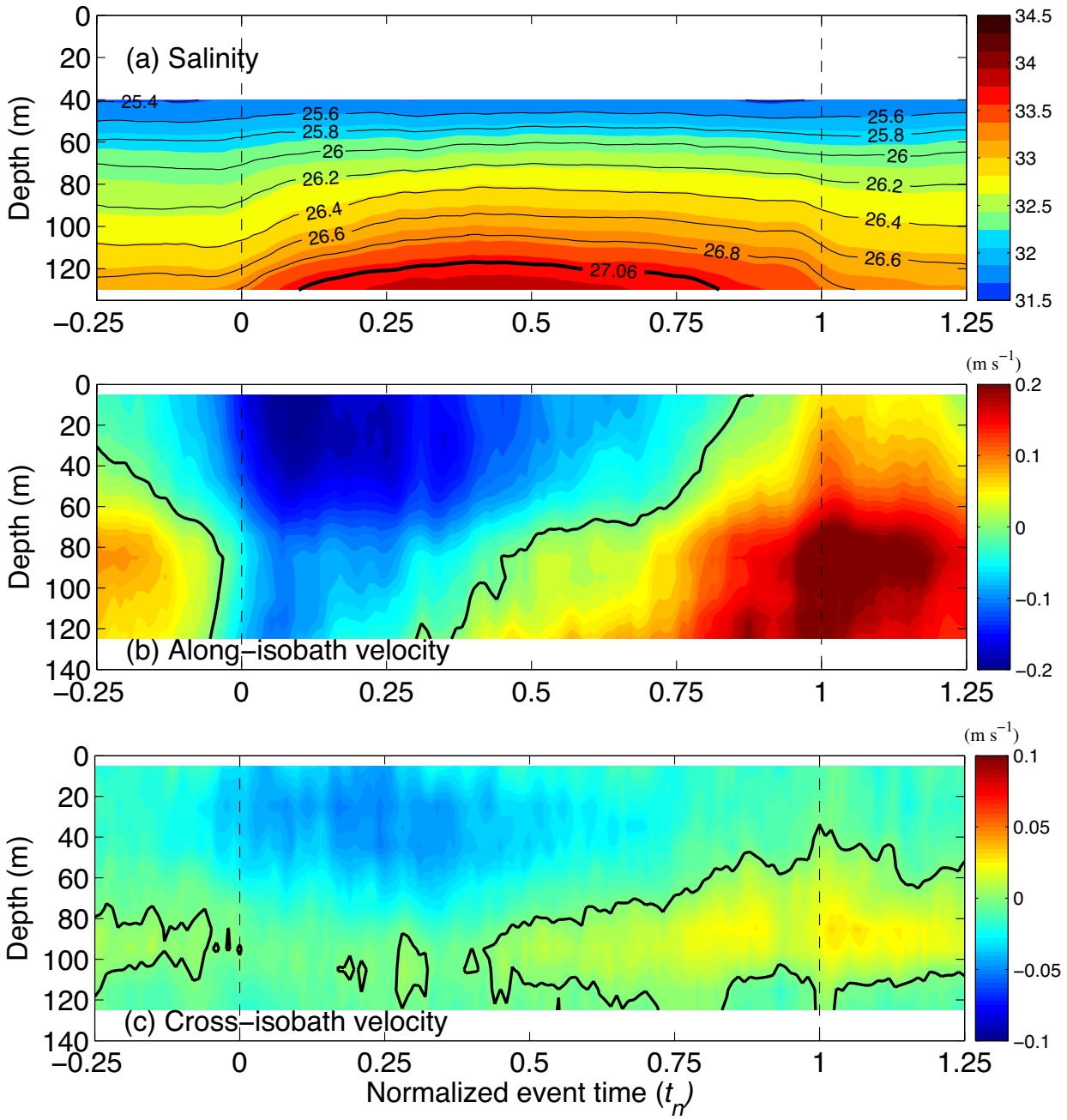

954

955 **Fig. 8.** Composite upwelling event constructed from the 85 individual AW-type upwelling events

956 from 2002 – 2004. (a) Salinity (color) overlaid by potential density (contours, kg m^{-3}). The thick

957 lines indicate the PW-AW interface. (b) Along-isobath velocity (positive is eastward). (c) Cross-

958 isobath velocity (positive is offshore). The 0 contours are highlighted.

959

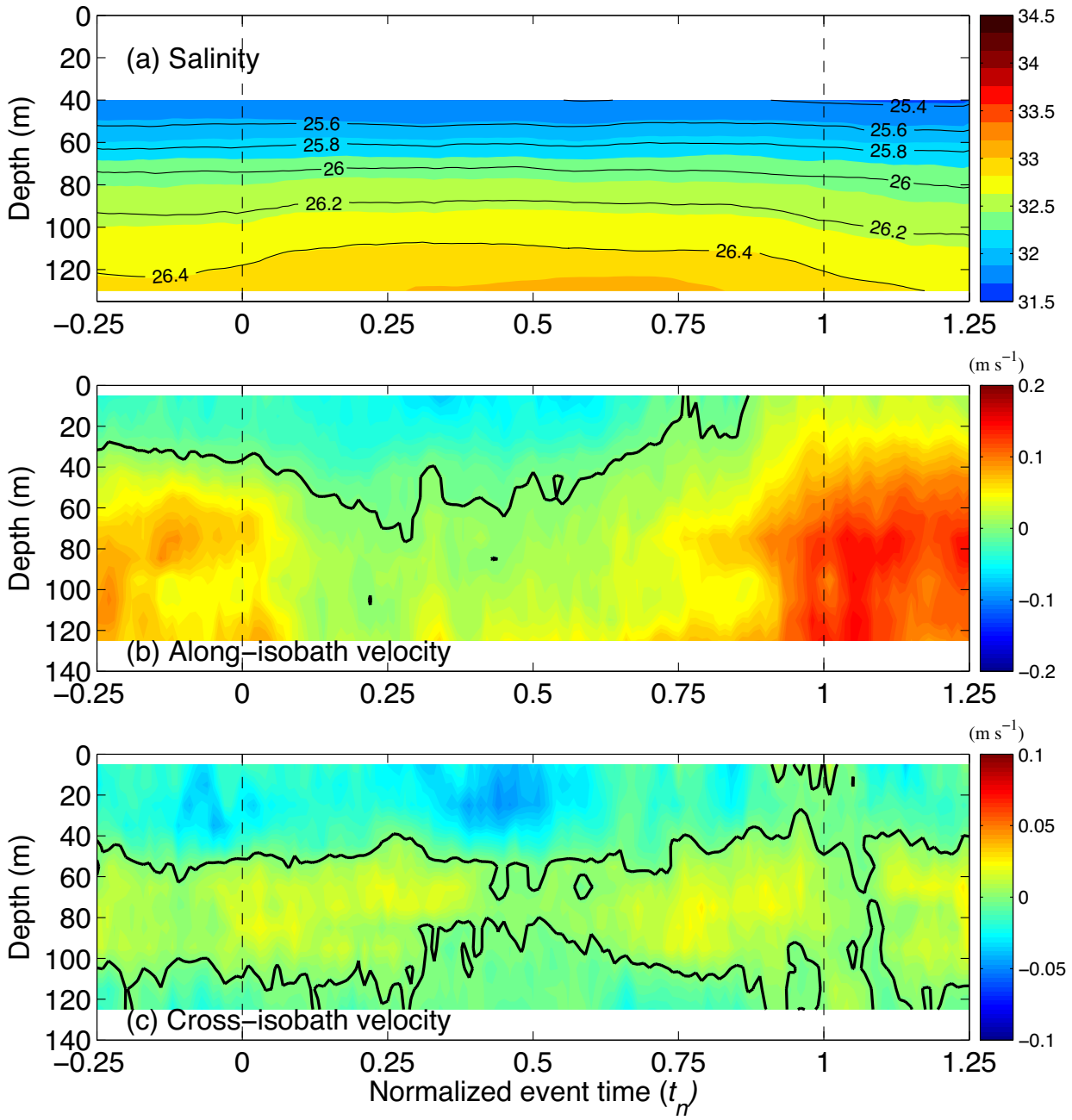

Fig. 9. Same as Fig. 8. except for the 30 PW-type upwelling events.

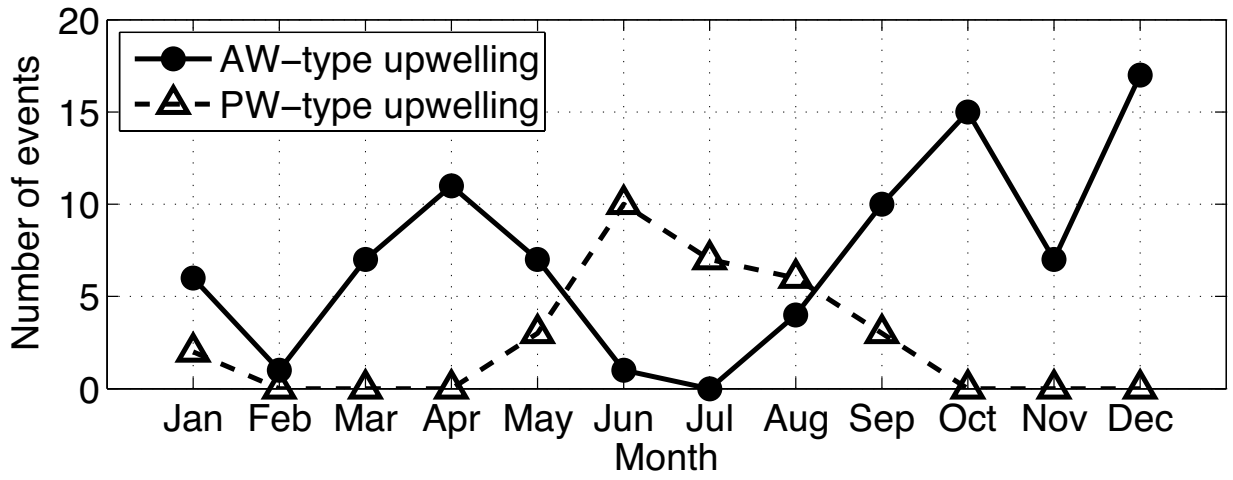

967

968 **Fig. 10.** Seasonal variation of the occurrence of AW-type upwelling events (solid line) and PW-

969 type upwelling events (dashed line).

970

971

972

973

974

975

976

977

978

979

980

981

982

983

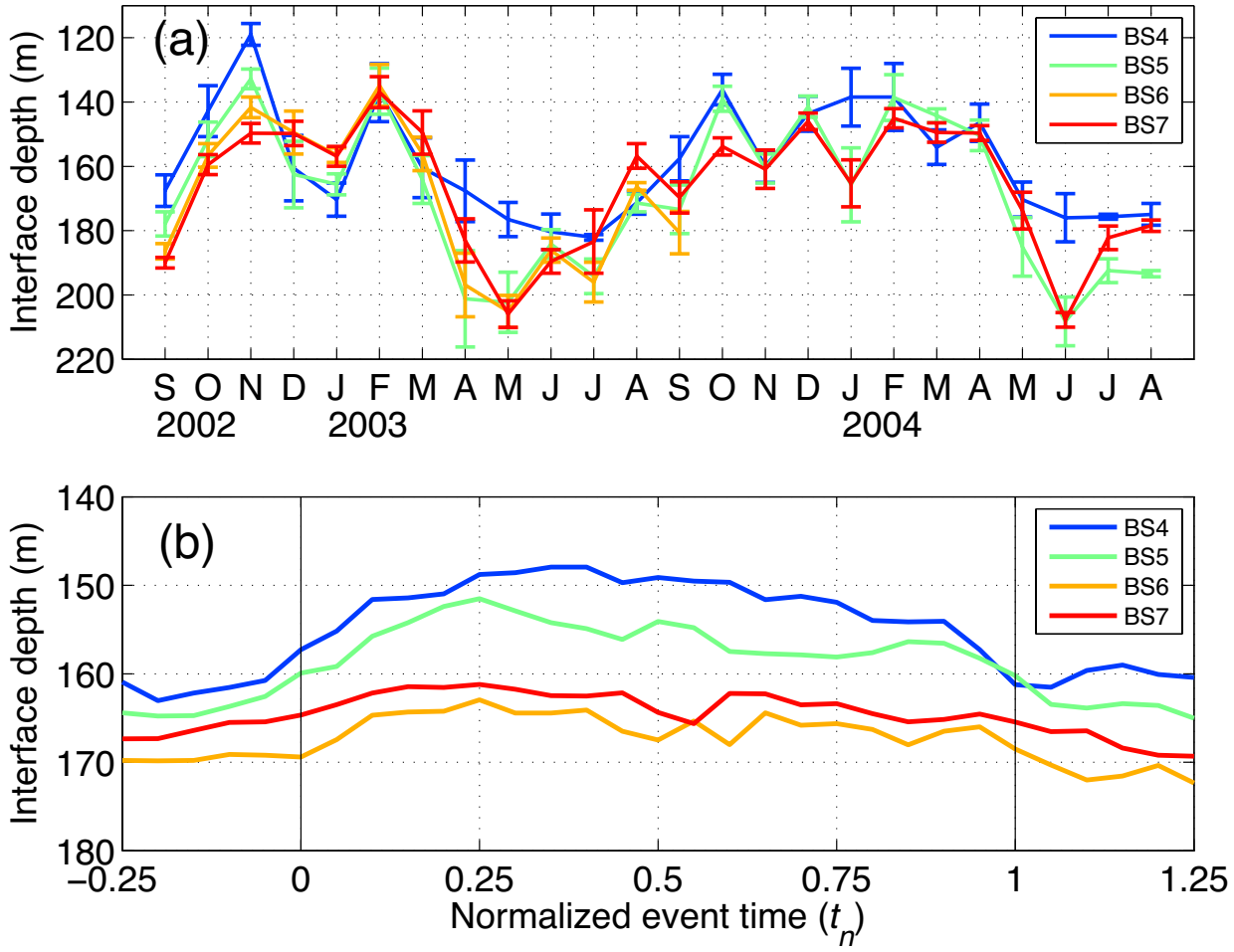

Fig. 11. (a) Timeseries of monthly-averaged PW-AW interface depth for the four offshore SBI moorings (2002 – 2004). The standard errors are indicated. (b) Interface depth for the composite upwelling event constructed using the SBI data, for each of the four moorings.

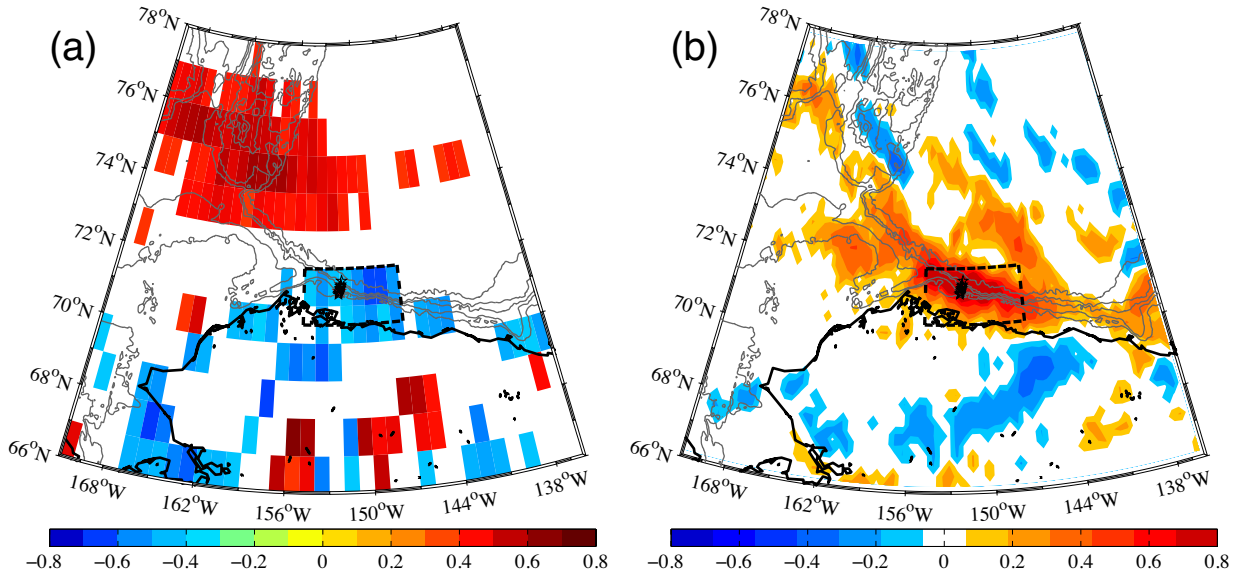

Fig. 12. Spatial distribution of correlation coefficient (points with confidence level < 95% are not plotted). (a) Wind stress curl at each point versus the PW-AW interface depth; (b) Wind stress curl at each point versus the wind stress curl close to mooring BS7. The dashed box delimits the region over which the wind stress curl was averaged for the calculations in the text. The black stars denote the mooring locations.

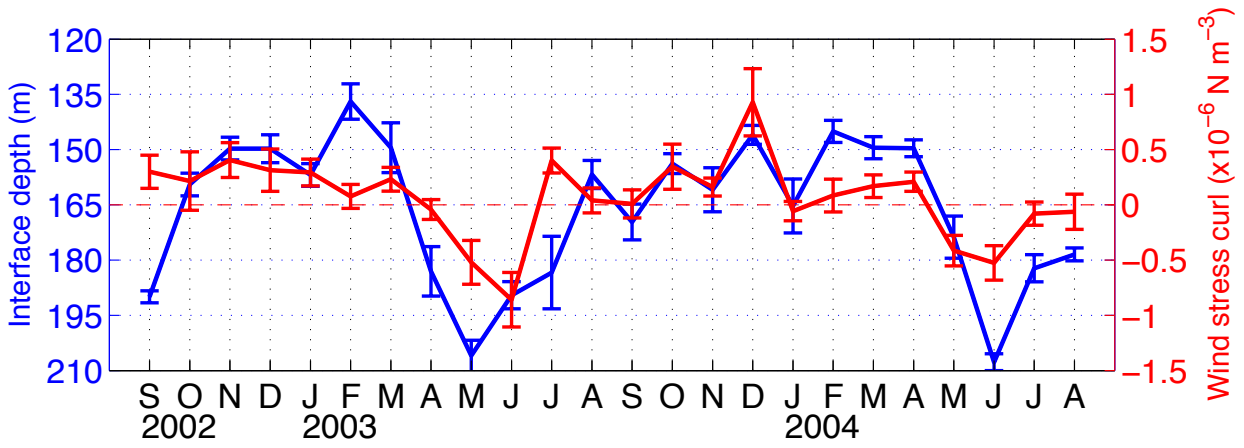

Fig. 13. Timeseries of monthly-averaged PW-AW interface depth (m, blue) and monthly area-averaged wind stress curl ($\times 10^{-6}$ N m^{-3}, red) for September 2002 – August 2004. The standard errors are included.

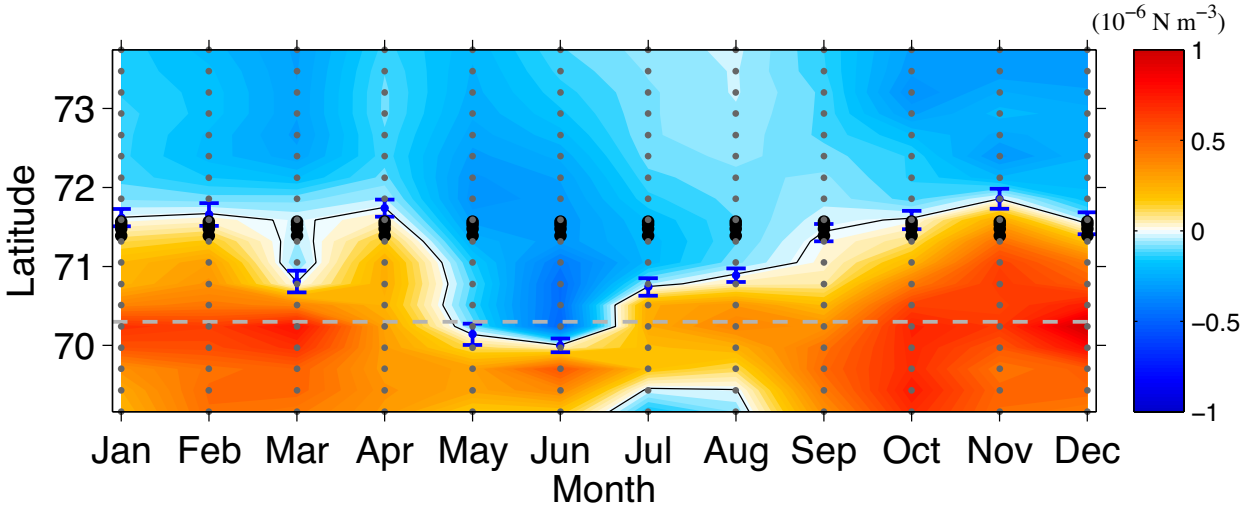

Fig. 14. Latitude-time distribution of the climatological monthly mean wind stress curl ($\times 10^{-6}$ N m^{-3}) close to 152°W for the time period 2000 – 2013. The zero-curl contour with standard error (blue bars) is highlighted. The grey dashed line marks the location of coastline, and the grey dots are ASR data points. Black dots denote the mooring locations.

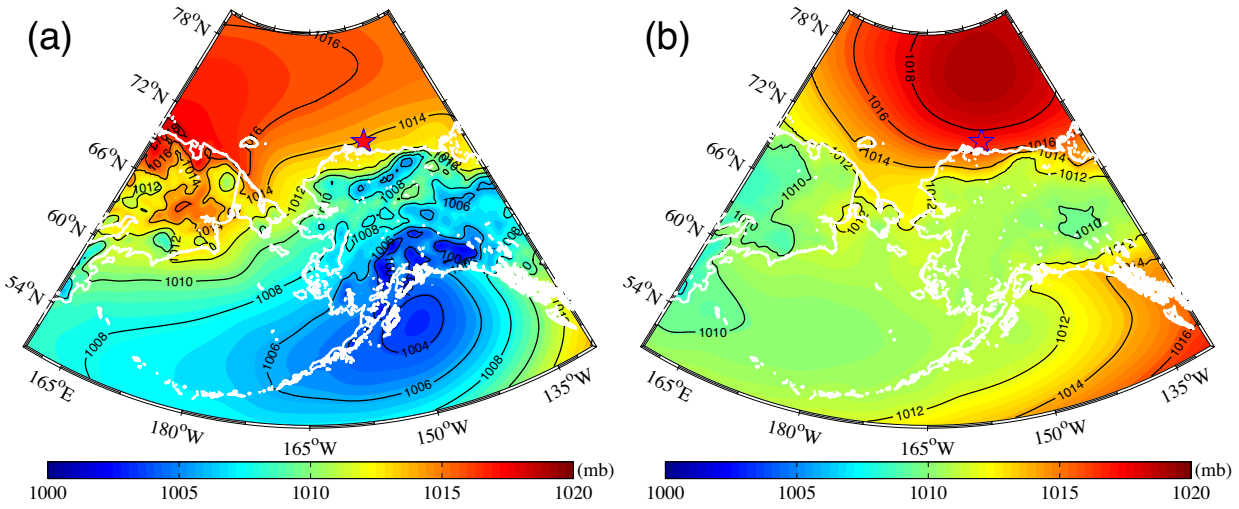

Fig. 15. Composite sea level pressure (mb) for the months when (a) the latitude of zero wind stress curl line is higher than the mean latitude plus one standard deviation, and (b) the latitude of zero wind stress curl line is lower than the mean latitude minus one standard deviation.